OPEN ACCESS
IMMT | IOP Publishing
International Journal of Extreme Manufacturing
Int. J. Extrem. Manuf. **8** (2026) 035004 (21pp)
https://doi.org/10.1088/2631-7990/ae3b82

Multiscale evolution of TiC particles in GH3536-based composites fabricated via laser powder bed fusion: coarsening mechanisms and hierarchical distribution

Peng Zhao[1], Quanquan Han[1,*], Zhenhua Zhang[1], Zhongyang Sui[1], Liqiao Wang[1], Bo Song[2], Min Zhu[1], Xiebin Wang[3], Rossitza Setchi[4] and Chuanzhen Huang[5]

[1] School of Mechanical Engineering, Shandong University, Jinan 250061, People's Republic of China
[2] School of Materials Science and Engineering, Huazhong University of Science and Technology, Wuhan 430074, People's Republic of China
[3] School of Materials Science and Engineering, Shandong University, Jinan 250061, People's Republic of China
[4] Cardiff School of Engineering, Cardiff University, Cardiff CF24 3AA, United Kingdom
[5] School of Mechanical Engineering, Yanshan University, Qinhuangdao 066004, People's Republic of China

E-mail: hanquanquan@sdu.edu.cn

Received 26 May 2025, revised 15 September 2025
Accepted for publication 21 January 2026
Published 9 February 2026

Abstract

The laser powder bed fusion (LPBF) of metal matrix composites (MMCs) involves distinctive rapid melting and nonequilibrium solidification dynamics. Elucidating the intricate evolution mechanisms of particles is critical for fabricating MMCs with superior strength-ductility synergy. In this study, both GH3536 Ni-based alloy and 5 wt% TiC-reinforced GH3536 composites (GH3536-5TiC) were fabricated via LPBF. The influence of volumetric laser energy density on the microstructure, mechanical properties, and multiscale evolution of TiC particles was systematically investigated. The experimental results revealed that a positive correlation existed between the energy density and both the TiC particle loss rate and average particle size, which was attributed to the coarsening and spattering behaviour of TiC particles, as demonstrated through multiscale evolution simulations. A dimensionless quantities framework based on kinetic calculations of the melt pool was established to determine the effect of energy density on TiC particle evolution. The growth mechanism of nanoscale TiC particles (<100 nm) is primarily governed by chemical transport, while microscale TiC particles (3–7 μm) mainly undergo impingement-driven coarsening. Low energy density was found to reduce the

* Author to whom any correspondence should be addressed.

impingement-driven coarsening. In addition, this study demonstrated the hierarchical distribution of TiC particles after multiscale evolution. Compared to GH3536, the GH3536-5TiC fabricated under low energy density conditions demonstrated significantly enhanced tensile performance. At 1 173 K, its ultimate tensile strength and elongation values were found to be 304 MPa and 42%, respectively. Overall, this work provides a theoretical guideline for the performance optimisation of additively manufactured advanced composites via controlling the evolution of reinforcements.

Supplementary material for this article is available online

Keywords: metal matrix composites, additive manufacturing, laser powder bed fusion, particle evolution, melt pool dynamics

1. Introduction

Metal matrix composites (MMCs) are a combination of reinforcements and metallic or alloy matrix materials[1]. MMCs are used in aerospace systems and extreme environments due to their excellent mechanical properties and superior thermal-mechanical stability. Laser powder bed fusion (LPBF) is one of the most widely utilised technologies in additive manufacturing (AM)[2], which employs a focused high-energy laser beam for layer-by-layer powder melting to generate 3D complex-shaped metallic components with relatively strong metallurgical bonding[3–5]. Compared to conventional fabrication methods, LPBF ensures that reinforcement particles are effectively integrated and uniformly dispersed within MMCs. Thus, LPBF offers a revolutionary solution for controllable manufacturing of MMCs.

In recent years, MMCs reinforced with carbides (WC, TiC, and SiC), borides (TiB_2 and ZrB_2), and oxides (Y_2O_3 and La_2O_3) have been successfully fabricated via LPBF[6–8]. Prior studies have predominantly investigated how particles regulate the composites' microstructural evolution and enhance mechanical performance[9–12]. GH3536 alloy (commercially known as Hastelloy X) is a solution-strengthened Ni-based superalloy that exhibits superior comprehensive properties below 1 173 K, including exceptional oxidation resistance, corrosion resistance, and fracture toughness[13]. This alloy has been widely employed in aeroengine combustion chambers, honeycomb structures, exhaust nozzles, and other hot-section components; it thus was considered to be an ideal matrix candidate for Ni-based composites[14]. The fabrication of GH3536-based composites via LPBF remains insufficiently explored, however, because the multiscale evolution mechanisms of the added reinforcements are not yet fully understood.

Generally, the mechanical properties of MMCs depend on the multiscale coordination of particle dispersion, interfacial reactions, and solidified microstructures. To improve the mechanical performance, researchers have pursued strategies to optimise the particles' dispersion[15,16], including modelling the particle motion within LPBF processes and elucidating dispersion mechanisms in LPBF-fabricated MMCs through both experimental work and multiphysical numerical modelling[17,18]. However, the multiphysical coupling between laser and powders generates very complex melt pool dynamics[19,20]. The high temperature gradients and rapid cooling rates strongly affect the thermodynamic stability of reinforcements, making it difficult to quantify the coarsening, dissolution, and reprecipitation behaviour. Although synchrotron X-ray imaging offers an advanced understanding of the transient melt pool behaviour[21–24], the direct inspection of particle evolution remains challenging, due to the limited phase contrast and the inherently two-dimensional nature of most imaging techniques. Recent studies on LPBF of oxide-dispersion-strengthened (ODS) alloys and TiC-reinforced steels have explored the oxide coarsening and TiC decomposition behaviour[25,26]. However, it still lacks a systematic energy density dependent framework that connects melt pool dynamics to the multiscale evolution of ceramic particles in Ni-based composites; the relationship between the multiscale evolution of reinforced particles and the mechanical properties of the fabricated components has not yet been fully understood. Thus, the research gap within LPBF of TiC-reinforced GH3536 composites lies in how to systematically reveal the multiscale evolution of TiC particles, and addressing the gap may benefit the precise fabrication of high-performance composites with tailored microstructure[27].

In this study, we fabricated TiC-reinforced GH3536MMCs via LPBF. Multiple characterisation techniques were employed in the quantitative analysis of TiC particle distributions/number variations under varying volumetric energy densities. The microstructural characteristics, precipitation behaviour, and mechanical properties of LPBF-fabricated specimens were also systematically investigated. Numerical simulation of melt pool dynamics was performed to analyse the multiscale evolution processes of TiC under high/low energy densities. Coupled with theoretical calculations of melt pool dynamics, the coarsening mechanisms of multiscale TiC during evolution pathways were further studied to reveal the hierarchical distribution patterns of TiC particles.

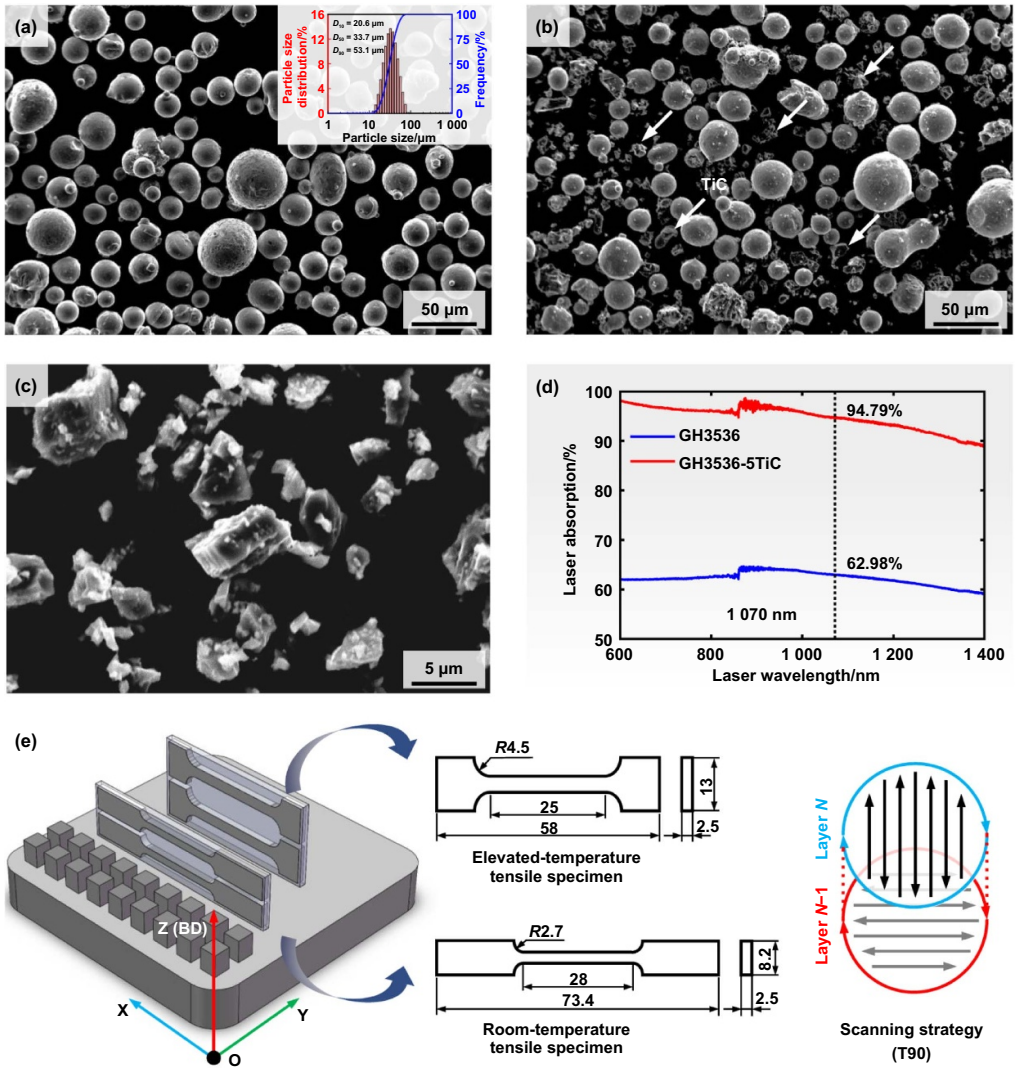

Figure 1. Details of the powder characteristics and LPBF process: (a)–(c) SEM images of GH3536 alloy powder, GH3536-5TiC composite powder and TiC powder, respectively; (d) laser absorption of GH3536 alloy powder and GH3536-5TiC composite powder; (e) dimensions of the tensile specimens and scanning strategy.

2. Experimental methods

2.1. Materials and LPBF process

Figure 1(a) presents the scanning electron microscopy (SEM) micrographs of gas-atomised GH3536 alloy powder. The chemical composition of GH3536 is listed in Table 1. Particle size characterisation was performed using a laser particle size analyser (Bettersizer 2600, Bettersize Instruments Ltd., China). The results indicate that the GH3536 alloy powder offers a particle size distribution of 20.6–53.1 μm with a D_{50} value of 33.7 μm. Irregular-shaped TiC particles, with a size distribution of 3–7 μm (the average particle size was approximately 5 μm) and purity of 99.5%, were employed in this study (Figure 1(c)). The microscale TiC particles rather than nanoscale particles were employed in this study, because the dispersion of nanoscale TiC is challenging and costly driven by high surface energy and van der Waals forces during the powder blending. The agglomerated nano TiC particles could easily cause the cracking defects during the LPBF process. The optimal addition of 5 wt% TiC was determined by considering both the LPBF formability and mechanical performance of the GH3536-based composites (Figure S1). A high-speed mixer (Hauschild SpeedMixer DAC 800.1 FVZ, Nordrhein-Westfalen, Germany) was employed to prepare GH3536-5 wt% TiC (GH3536-5TiC) feedstock. To ensure homogeneous mixing, eight blending cycles were conducted using a high-speed mixer at 1 100 rpm for 1.5 min per cycle. Intermittent cooling to 298 K was implemented between successive mixing cycles to prevent thermal accumulation. The SEM image in Figure 1(b) shows uniformly dispersed TiC particles within the GH3536-5TiC composite powder. Figure 1(d) reveals the enhanced laser absorption characteristics of GH3536-5TiC composite powder at a wavelength of 1 070 nm. The measured absorption rates for GH3536 alloy and GH3536-5TiC composite powder were 62.98% and 94.79%, respectively.

Table 1. Chemical composition of GH3536 alloy powder (wt%).

	C	Ti	Cr	Fe	Mo	Co	W	Si	Al	Ni
GH3536	0.07	0.01	22.15	19.16	8.87	1.64	0.54	0.03	0.06	Bal.

Table 2. LPBF process parameters used in this study.

Type	Values
Shielding gas	Argon
GH3536 alloy powder size/μm	$D_{10} = 20.6$, $D_{50} = 33.7$, $D_{90} = 53.1$
TiC particle size/μm	3–7
Laser power/W	190
Layer thickness/μm	30
Hatch spacing/μm	70, 90, 110
Laser scanning speed/(mm·s^{-1})	600, 800, 1 000, 1 200

All specimens were fabricated using a Concept Laser Mlab Cusing 200 R system (GE Additive, Germany) under an argon atmosphere. A zigzag T90 scanning strategy was employed, along with 90° interlayer rotation between successive layers (Figure 1(e)). Cubic specimens (6 mm × 6 mm × 7 mm) were fabricated with varying laser scanning speeds and hatch spacing to investigate the effects of energy density on TiC evolution and microstructure. The LPBF process parameters used in this study are shown in Table 2. Tensile specimens for both ambient temperature (298 K) and elevated temperature (1 173 K) testing were fabricated to investigate the influence of energy density on mechanical properties. Identical LPBF process parameters were used for both tensile and cubic specimens, and Figure 1(f) illustrates the geometry and dimensions of the tensile specimens. The volumetric energy density (ρ_V) may be expressed as[28]:

$$\rho_V = \frac{p_L}{S_s \cdot H_s \cdot T_L} \tag{1}$$

where P_L is the laser power, S_S is the laser scanning speed, H_S is the hatch spacing, and T_L is the layer thickness.

2.2. Material characterisation techniques

The planes parallel to the build direction (BD) in cubic specimens were ground and polished for microstructural characterisation. Electrochemical etching with a 15% oxalic acid solution at 3.3 V was performed on cubic specimens to reveal precipitates and subgrains in the composite. Microstructure analysis was conducted via optical microscopy (OM), scanning electron microscopy (SEM; JSM-7800F, Jeol) equipped with energy-dispersive X-ray spectroscopy (EDX), and electron backscatter diffraction (EBSD) systems. Backscattered electron (BSE) and secondary electron (SE) images were acquired at accelerating voltages of 20 kV and 10 kV, respectively. The average particle size and number of TiC were statistically analysed using ImageJ software. EBSD mapping was performed with a step size of 1 μm, covering an area of 800 μm × 800 μm per cubic specimen. EBSD data were processed using HKL Channel 5 software for crystallographic orientation analysis. Phase identification was carried out by X-ray diffraction (XRD; SmartLab 3 kW, Rigaku, Japan). Scans were performed using Cu Kα radiation at a rate of 3°·min^{-1} over a 2θ range of 30°–100°. An ion milling equipment (Gatan 695, Pleasanton, USA) was used for processing specimens prior to transmission electron microscopy (TEM) inspection. A TEM (FEI F200X TALOS, Thermo Fisher, USA) was employed to further investigate the microstructure of the specimens. Ambient temperature tensile tests were conducted using a universal testing machine (Zwick-Z250, Zwick Roell, Germany) at a strain rate of 0.04 min^{-1}. Elevated temperature tensile tests were performed using a high-temperature testing system (QJ212, Qingji, China) with a strain rate of 0.1 min^{-1}.

2.3. Numerical modelling

Computational fluid dynamics (CFD) simulations were conducted based on a developed single-track three-dimensional transient model[29] to investigate the thermophysical behaviour of melt pools and TiC particles evolution. EDEM was employed to simulate the generation and motion of powder particles. The powder bed model is shown in Figure 2(a). Both the substrate and matrix material were GH3536. The GH3536 alloy powder had a normal particle size distribution ranging from 15 μm to 53 μm. The TiC powder (5 wt%) exhibited a normal particle size distribution between 3 μm and 7 μm. These parameters were integrated into ANSYS Fluent using a user-defined function (UDF) to solve a transient fluid dynamics model. Figure 2(b) illustrates the entire computational domain of the model, which was divided into two regions: a powder-gas layer (1 000 μm × 400 μm × 100 μm) and a substrate layer (1 000 μm × 400 μm × 100 μm). Structured grids were automatically generated in Fluent by specifying the grid type and parameters. The computational domain was discretised into hexahedral structured meshes with a uniform element size of 1 μm, as illustrated in Figure 2(b). The top boundary was modelled as a pressure-outlet with ambient pressure (1 atm) while the bottom boundary was a no-slip wall. The nonequilibrium solidification paths of GH3536 superalloy were calculated using the Gulliver-Scheil solidification model in Thermo-Calc. Additionally, the thermophysical properties of GH3536 were determined using the Thermo-Calc. Table 3 summarises the key physical properties of the GH3536 alloy and TiC particles used in the study.

In this study, the following basic assumptions were made for the CFD model[34]:

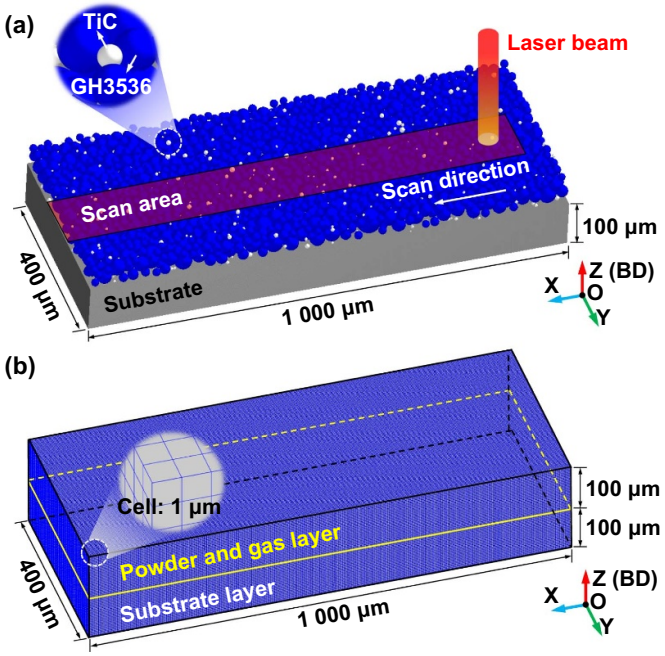

Figure 2. Schematic of the simulation model and computational domain: (a) powder bed model established using EDEM software; (b) complete computational domain comprising powder-gas and substrate layers with a mesh size of 1 μm.

(1) The gas and liquid phases are treated as incompressible Newtonian fluids.
(2) The compositional changes caused by evaporation are ignored.
(3) The laser absorption rate of composite materials is constant.
(4) The thermal properties of the material are constant.

The mass equation is[34]:

$$\frac{\partial C_k}{\partial t} + \nabla \cdot \left(C_k \vec{U} \right) = \dot{m}_k \tag{2}$$

where C_k represents the mass concentration of element k, and the mass source term for this element is introduced as $\dot{m}_k$. The $\vec{U}$ is the fluid velocity.

The momentum conservation equation is expressed as[34]:

$$\frac{\partial \left(\rho \vec{U} \right)}{\partial t} + \nabla \cdot \left(\rho \vec{U} \vec{U} \right) = \nabla \cdot S + \rho \vec{g} + \sum_k \dot{m}_k \vec{u}_k \tag{3}$$

where $\boldsymbol{S}$ is the fluid stress tensor, ρ, $\vec{u}_k$, and $\vec{g}$ refer to the fluid density, velocity of the mass source for k, and the gravitational acceleration, respectively.

The thermal energy equation is:

$$\frac{\partial (\rho I_f)}{\partial t} + \nabla \cdot \left(\rho I_f \vec{U} \right) = -p \left(\nabla \cdot \vec{U} \right) + \nabla \cdot (K \nabla T) + \sum_k \dot{m}_k I_k + Q_f \tag{4}$$

where T is the temperature of fluid, K is the thermal conductivity of fluid, I_f and I_k denote the internal energy of the fluid and of element k (from the mass source), respectively. Q_f is the volumetric heat source absorbed.

The melt pool free surface is tracked using the Volume of Fluid (VoF) method[35]:

$$\frac{\partial F}{\partial t} + \nabla \cdot \left(F \vec{U} \right) = \sum_k \frac{\dot{m}_k}{\rho_k} \tag{5}$$

where F represents the volume fraction of the liquid phase.

The Marangoni force equation is[34]:

$$\vec{f}_t = -\frac{d\gamma}{dT} \left[\nabla T - (\nabla T . \vec{n}) \vec{n} \right] \tag{6}$$

where γ is the interface energy.

The wetting force equation is[34]:

$$\vec{f}_w = \gamma_{\mathrm{lg}} \left(cos\theta - cos\theta_e \right) \vec{t} \tag{7}$$

where γ_{lg} is the liquid–gas interface energy, the angles θ and θ_e correspond to the current and equilibrium contact angles at the interface, respectively. $\vec{t}$ is the unit vector normal to the contact line on a particle.

The Gaussian heat source equation is[36]:

$$Q = \frac{2AP_L}{\pi r_0^2} exp \left(-\frac{2r^2}{r_0^2} \right) \tag{8}$$

where A is absorptivity, r_0 is the radius of the laser spot, r is the radial distance from the laser centre.

3. Results

3.1. TiC particle characterisation

Figure 3 illustrates the microstructure of both GH3536 Ni-based alloy and GH3536-5TiC composite fabricated via LPBF. Under the optimum condition of 1 200 mm·s^{-1} scanning speed and 110 μm hatch spacing, some keyholes were detected in the GH3536 alloy, with the relative density reaching 99.7% (Supplementary Figure S2). Differentiated fabrication of GH3536-5TiC composites under varying energy densities was achieved by controlling scanning speed (600–1 200 mm·s^{-1}) and hatch spacing (70–110 μm). Both OM and low-magnification SEM analysis demonstrate improved LPBF formability in TiC-reinforced GH3536, with the absence of cracks or fusion defects across varying process parameters (Figures 3(b)–(d)). The relative densities of all the LPBF-fabricated GH3536-5TiC composites were above 99.2% with a maximum value of 99.8% (Supplementary Figure S2). Abundant irregular TiC particles were observed in composites, which confirms the effectiveness of LPBF in achieving microscale TiC particle addition. Notably, the energy density exerts significant influence on both the number density and spatial arrangement of TiC particulates. The amount of TiC in low energy density specimens (45 J·mm^{-3},

Table 3. Material properties and related coefficients used in the simulation[30–33].

Material	Property	Value	Unit
GH3536	Density	8 340	$kg{\cdot}m^{-3}$
	Solidus temperature	1 537	K
	Liquidus temperature	1 649	K
	Specific heat capacity	0.43–0.78 (300–3 500 K)	$J{\cdot}g^{-1}{\cdot}K^{-1}$
	Thermal conductivity	12.05–31.60 (300–3 500 K)	$W{\cdot}m^{-1}{\cdot}K^{-1}$
	Dynamics viscosity	$(1.26–0.24) \times 10^{-2}$ (1 537–3 500 K)	Pa·s
	Diffusion coefficient	$(3.23–5.99) \times 10^{-6}$ (300–3 500 K)	$m^2{\cdot}s^{-1}$
	Surface tension	1.81	$N{\cdot}m^{-1}$
	Molar volume	7.79×10^{-6}	$m^3{\cdot}mol^{-1}$
TiC	Density	4 880	$kg{\cdot}m^{-3}$
	Melting point	3 300	K
	Thermal conductivity	21.23	$W{\cdot}m^{-1}{\cdot}K^{-1}$
	Specific heat capacity	0.89	$J{\cdot}g^{-1}{\cdot}K^{-1}$
	Diffusion coefficient	5.50×10^{-9}	$m^2{\cdot}s^{-1}$
	Molar volume	1.21×10^{-5}	$m^3{\cdot}mol^{-1}$

GH3536-TL) demonstrates marked enhancement compared to high energy density specimens (143 $J{\cdot}mm^{-3}$, GH3536-TH). Note that, the solid (GH3536 powder/TiC particle) spatter occurred and cannot be avoided under all LPBF conditions. Reducing the laser energy density, however, could decrease the vapor jet intensity, preventing more solid spatters from being ejected[37]. Under high laser energy density conditions, the loss of TiC particles may result from solid spatters caused by the vapor jet interacting with solid powder outside the laser interaction regions; this behaviour is further discussed in Section 4.1.

Six noncontinuous observation areas were selected on the XOZ plane of specimens fabricated under distinct processing parameters. High-contrast microstructural features were captured using BSE, as illustrated in Figure 4(a). EDX elemental mapping (Figure 4(b)) confirmed that the irregular black microscale particles were TiC particles. Due to the low planar lattice disregistry between TiC and GH3536[38], no interface failure characteristics, such as cracks, were observed at the bonding edge between TiC and the matrix.

Threshold segmentation was performed using ImageJ software to quantify TiC particles with diameters larger than 500 nm (Figures 4(c)–(e)). Statistical evaluations included TiC particle number and average equivalent diameter. In the GH3536-TL specimen, the TiC particle number reached approximately 1.31×10^4, while the GH3536-TH specimen exhibited a lower value of 0.37×10^4. In the GH3536-TH specimen, the average TiC particle size was measured at 3.98 μm, while the GH3536-TL specimen offered a lower value of 3.55 μm, as shown in Figures 4(c) and (d). As shown in Figure 4(e), when the energy density increased from 45 $J{\cdot}mm^{-3}$ to 143 $J{\cdot}mm^{-3}$, the TiC particle number decreased by 72%. Concurrently, the average TiC particle size increased by 12%. The experimental data demonstrates a concurrent occurrence of TiC particle loss and size coarsening under elevated energy density conditions.

3.2. Microstructure characterisation

To further analyse the TiC particles distribution and evolution, the as-built specimens were unetched and analysed using the BSE imaging. As shown in Figures 5(a) and (b), a large number of nanoscale near-spherical dark and bright phases were observed in both GH3536-TH and GH3536-TL specimens (Figures 5(c)–(f)). The EDX point analysis (Table 4) indicated that the nanoscale dark regions were enriched in Ti and C (EDX Point 2), while the nanoscale bright regions were enriched in Mo, Ti, and C (EDX Point 3). Previous study has shown that during the LPBF fabrication of MMCs, the complex fluid flow induced by thermal gradients in melt pools could break up the ceramic particles into nanoscale and disperse them in the matrix[39]. This implies that the nanoscale near-spherical dark phases might be TiC particles, and the nanoscale bright phases could be carbide precipitates[40]. Interestingly, a size discrepancy of nanoscale TiC particles was observed under the high/low energy density conditions. That is, the nanoscale TiC particles coarsening occurred in the GH3536-TH specimen and the distribution of TiC particles was found to be more homogeneous compared to the GH3536-TL specimen (Figures 5(d) and (f)) under the higher resolution BSE inspections. This behaviour may be explained by the spatial variations in Marangoni convection intensity and local cooling rates during the LPBF process[41].

Microstructural analysis was performed on etched GH3536, GH3536-TH, and GH3536-TL specimens to investigate the precipitation phases under varying energy densities. As shown in Figures 6(a) and (b), SEM images reveal epitaxially grown cellular substructures along the BD during rapid solidification in GH3536, with dendritic arm spacing measuring approximately 500 nm. As shown in Figures 6(c) and (d), compared to GH3536, the addition of TiC particles generated more dendritic structures in the GH3536-TH, with the dendritic arms displaying noticeable wavy curvatures. The

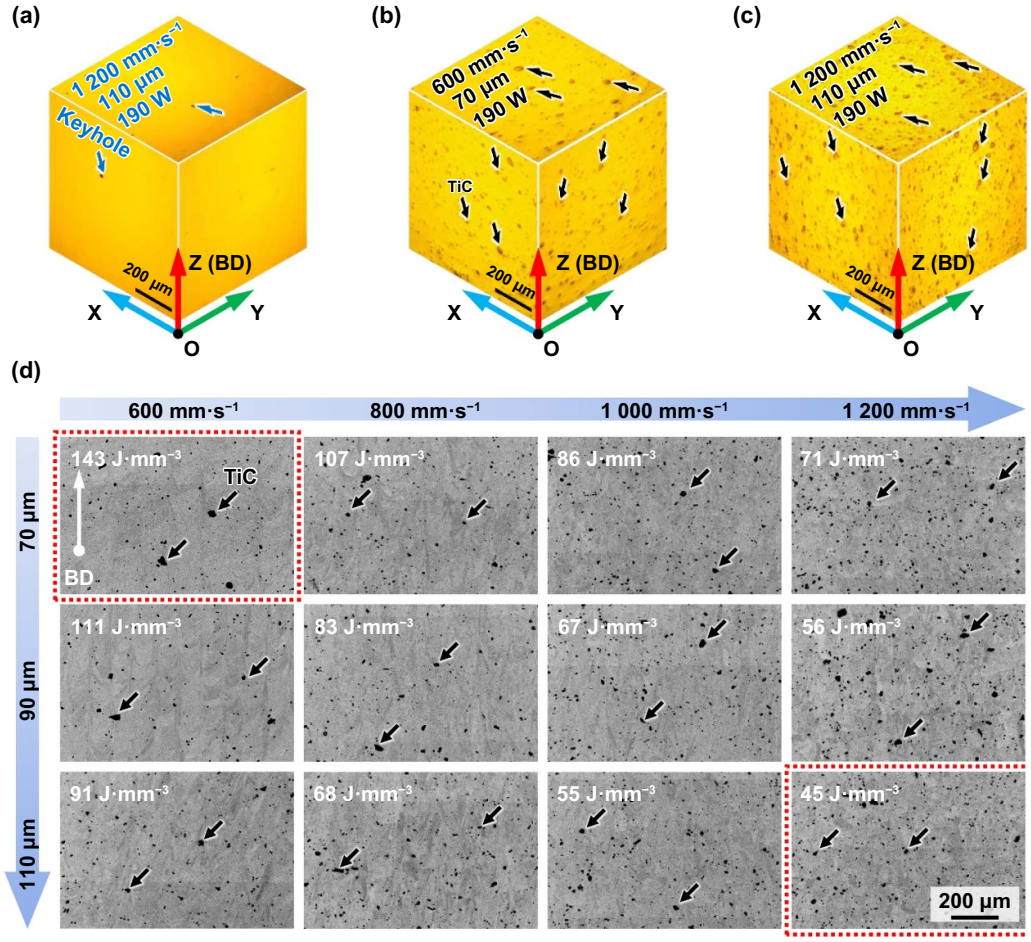

Figure 3. OM and BSE images of LPBF-fabricated specimens: (a) OM images of GH3536 alloy; (b) and (c) OM images of GH3536-5TiC composite; (d) cross sectional BSE images of GH3536-5TiC composite.

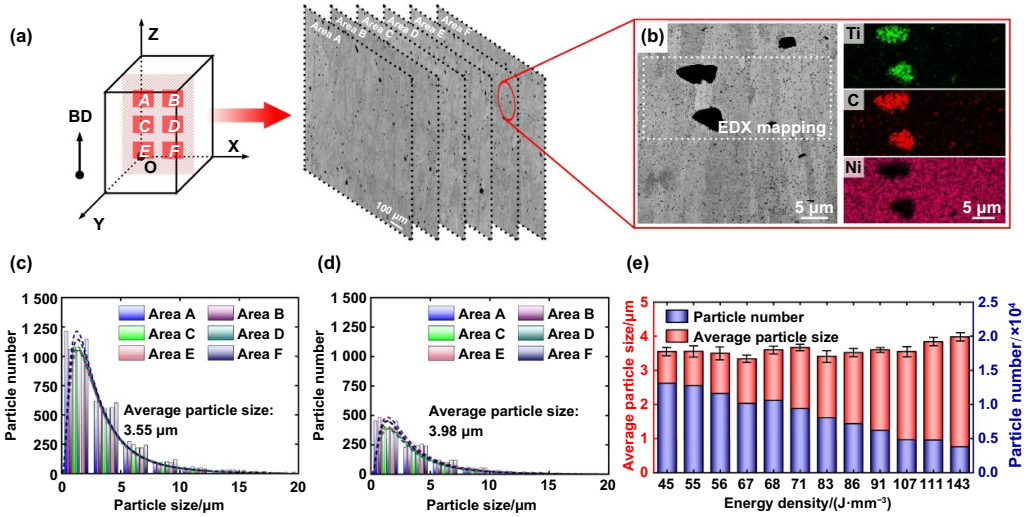

Figure 4. Quantitative analysis of TiC particles in GH3536-5TiC composites: (a) schematic diagram of the statistical area's BSE micrograph; (b) micrograph and EDX mapping of the area highlighted in (a) at high magnification; statistical diagrams of TiC particle size distribution in (c) GH3536-TL and (d) GH3536-TH; (e) statistical diagram of average particle size and TiC particle number in specimens fabricated with different energy densities.

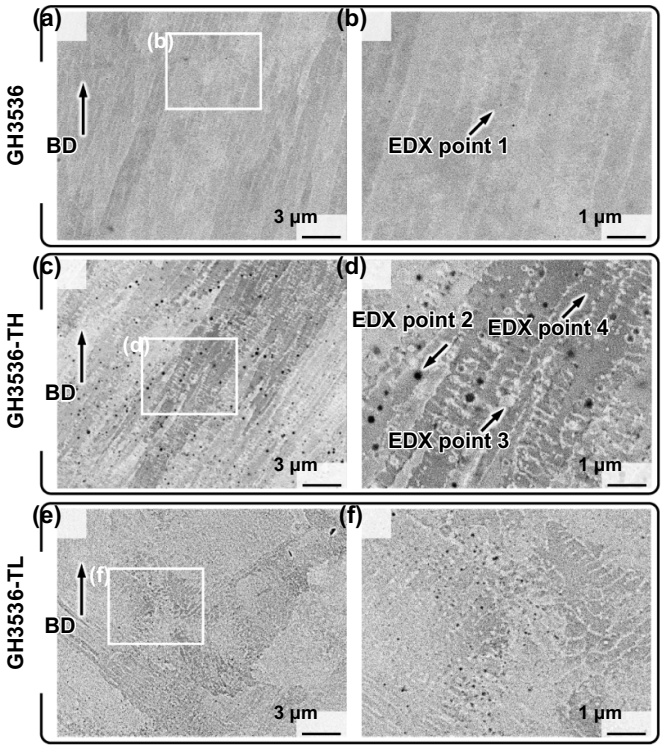

Figure 5. BSE micrographs of unetched specimens: (a) and (b) GH3536; (c) and (d) GH3536-TH; (e) and (f) GH3536-TL.

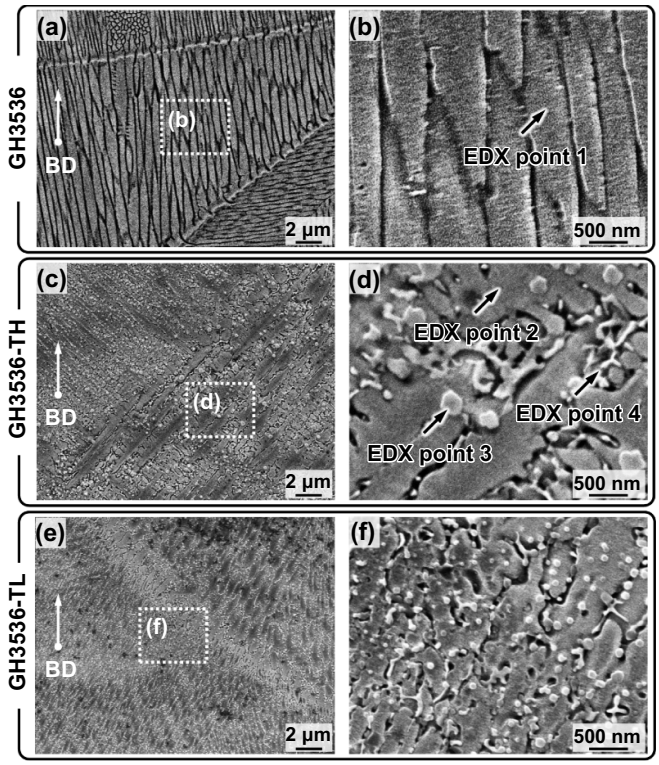

Figure 6. SEM characterisation of etched specimens: (a) and (b) GH3536; (c) and (d) GH3536-TH; (e) and (f) GH3536-TL.

Table 4. Results of EDX point analysis.

	Content of elements/wt%			
EDX point number	Cr	Mo	Ti	C
1	21.5	8.2	0.0	0.0
2	21.2	8.1	5.2	3.9
3	21.6	8.8	4.5	3.7
4	21.6	8.3	1.2	0.9

Table 5. Results of EDX point analysis.

	Content of elements/wt%			
EDX point number	Cr	Mo	Ti	C
1	22.1	8.4	0.0	0.0
2	21.8	8.5	0.8	0.0
3	21.9	9.6	3.9	3.6
4	22.2	9.8	3.7	3.2

heterogeneous nucleation effect of TiC particles facilitated dendritic arm development. Compared to GH3536-TH, GH3536-TL exhibits distinctive asymmetric dendritic structures (Figures 6(e) and (f)) characterised by irregular dendritic arms and reduced arm spacing. This phenomenon is primarily attributed to the higher cooling rates within the low energy density melt pools, where dendritic growth becomes constrained, resulting in irregular microstructures.

The morphology and compositional changes of the precipitate phases were systematically studied through both SEM and EDX point analysis. No significant secondary phase precipitates were observed in GH3536 in Figures 6(a) and (b). As shown in Figures 6(c)–(f), both GH3536-TH and GH3536-TL specimens exhibit bimodal precipitation patterns (within dendrites and between dendrites). The precipitates within the dendrites of GH3536-TH exhibit a square morphology. In contrast, GH3536-TL displays a near-spherical morphology within dendrites, alongside a marked increase in spatial density. The precipitate phases between the dendrites exhibit a continuous network shape as well as discontinuous irregular shapes. These differences could be attributed to variations in the melt pool cooling time. As shown in Table 5, the Mo and Ti content in GH3536-TH is higher than that of GH3536. Ti and Mo enrichments were detected in both the precipitates and the surrounding GH3536 matrix, indicating that the enrichments were likely to be (Mo, Ti)C carbides[42]. In fact, the spot of electron beam is determined by its acceleration voltage so that the control of the accelerating voltage is essential for characterizing small particles. Otherwise, the spot may cover both the particle and the matrix. Hence, the obtained result is the combined compositions of both the particle and the matrix in the spot. To further determine the carbides composition, a TEM examination is conducted and the results are systematically analysed in Figure 9.

As shown in Figure 7, EBSD analysis of the LPBF-fabricated specimens was conducted. The results reveal columnar grain formation in GH3536 (Figure 7(a-i)). A dominant <001> crystallographic orientation was observed along the BD, and the inverse pole figure (IPF, Figure 7(a-iv)) exhibited a maximum texture density (MTD) value of 5.49. Due

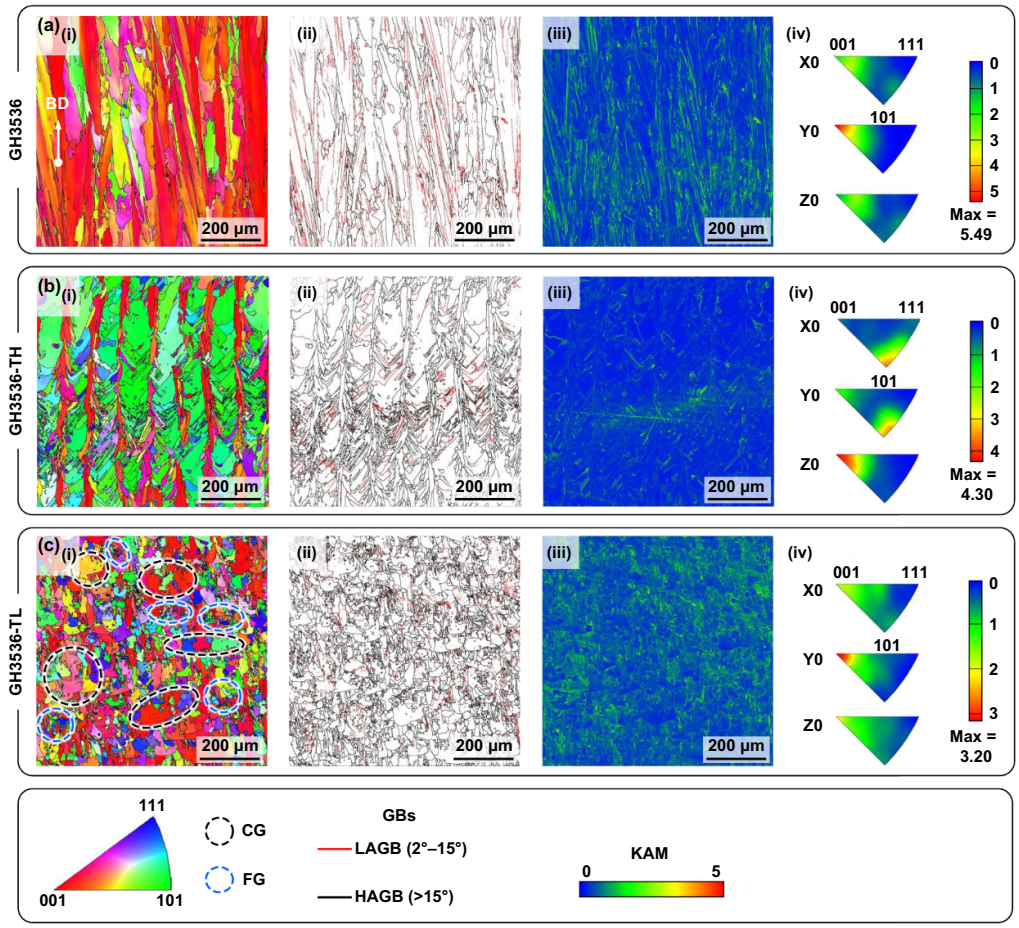

Figure 7. The EBSD results of LPBF-fabricated specimens: (a) GH3536: (a-i) inverse pole figure (IPF) Y maps, (a-ii) grain boundary (GB) distribution maps, (a-iii) kernel average misorientation (KAM) distribution maps, (a-iv) IPF maps; (b) GH3536-TH: (b-i) IPF Y maps, (b-ii) GB distribution maps, (b-iii) KAM distribution maps, (b-iv) IPF maps; (c) GH3536-TL: (c-i) IPF Y maps, (c-ii) GB distribution maps, (c-iii) KAM distribution maps, (c-iv) IPF maps. The black lines denote high-angle grain boundary (HAGB) and the red lines denote low-angle grain boundary (LAGB).

to the high temperature gradient ($\sim 10^7$ K·m^{-1}) during the LPBF process, the growth direction of columnar grains aligns with the heat flow direction[43]. The TiC addition reduced the <001> texture intensity in the GH3536-TH specimen (Figure 7(b-i)) with red regions partially being replaced by green regions; the calculated MTD values decreased from 5.49 to 4.3 (Figure 7(b-iv). Reducing the laser energy density witnessed a further reduction of the texture from 4.3 to 3.2 in the GH3536-TL (Figures 7(c-i) and (c-iv)), implying that changing the energy density within LPBF was a feasible path in tailoring the texture. Note that the GH3536-TH specimen still exhibited strong texture, but its MTD value was examined to be reduced compared to the GH3536 alloy, suggesting that the TiC-induced heterogeneous nucleation played a key role in reducing the composite material's texture. As for GH3536-TH and GH3536-TL specimens, the GH3536-TL specimen offered weaker texture because a higher scanning speed caused a shorter melt pool duration time and freezing range so that the formed grains were more equiaxed in the GH3536-TL specimen[44].

The distribution maps of grain boundary misorientation are shown in Figure 8(a). For GH3536, low-angle grain boundaries (LAGBs, $\theta < 15°$) constituted 75%. After adding TiC, the proportion of high-angle grain boundaries (HAGBs, $\theta > 15°$) in the GH3536-TH and GH3536-TL specimens increased to 65% and 49%, respectively. The phenomenon could be attributed to two factors. First, the localised stress concentration at TiC/GH3536 interfaces promotes dislocation climb, accelerating subgrain coalescence[45]. Second, TiC particles accommodate part of the plastic strain, thereby facilitating the transformation of LAGBs to HAGBs.

An approximately equiaxed grain structure formed with an average size of 10.69 μm, as shown in Figure 8(b); the grain size of GH3536-TL was refined by 63% compared to GH3536 (29.28 μm) and by 19% compared to GH3536-TH (13.23 μm). This phenomenon may be attributed to two factors. First, the growth of columnar crystals might have been suppressed by heterogeneous nucleation through TiC particles (Figure 5); the local segregation of Ti and C elements formed a compositional supercooling zone, promoting the transition

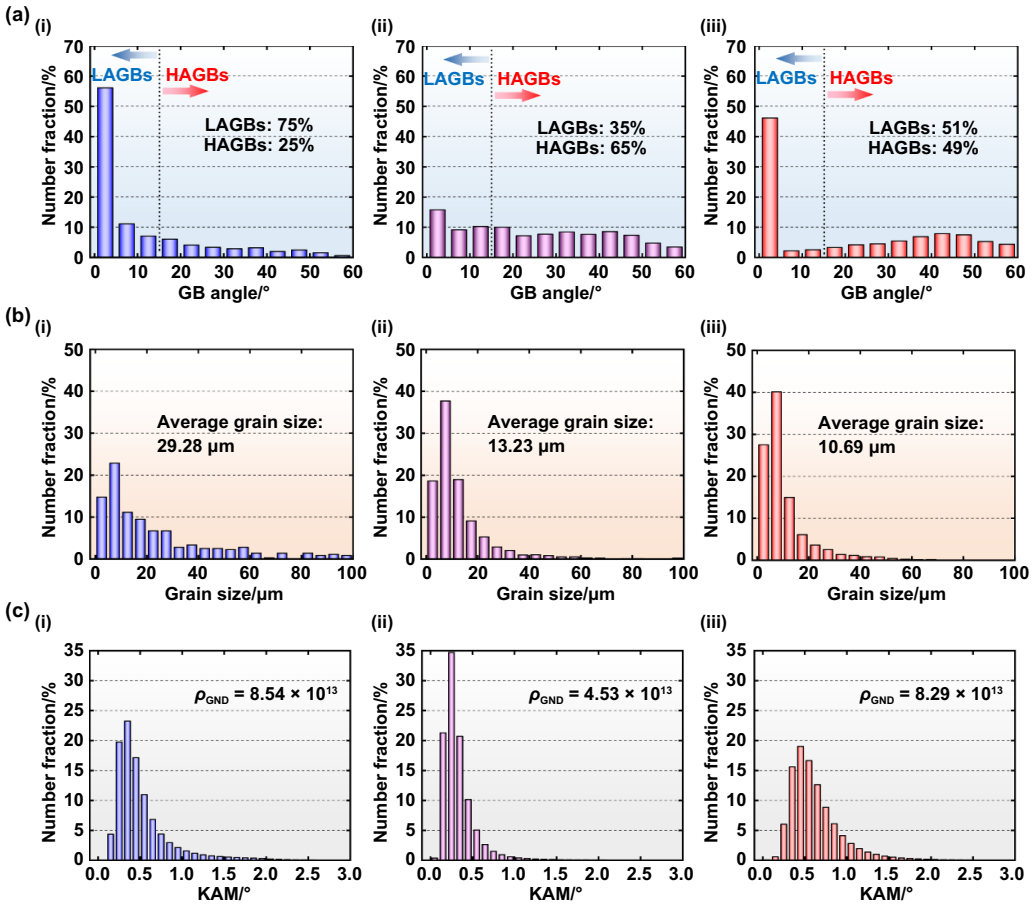

Figure 8. The EBSD analysis results of LPBF-fabricated specimens: (a) the distribution maps of grain boundary misorientation: (a-i) GH3536, (a-ii) GH3536-TH, (a-iii) GH3536-TL; (b) the distribution maps of grain size: (b-i) GH3536, (b-ii) GH3536-TH, (b-iii) GH3536-TL; (c) the distribution maps of GND density: (c-i) GH3536, (c-ii) GH3536-TH, (c-iii) GH3536-TL.

from columnar to equiaxed crystals. Second, the high laser absorptivity (∼94.8%) of the composite material increased the solid-liquid interface perturbations, disrupting crystal orientation consistency. Interestingly, after reducing the energy density, GH3536-TL exhibited a bimodal structure consisting of fine grains (FGs) and coarse grains (CGs) (Figure 7(c-i))[44].

As shown in Figure 8(c), the geometrically necessary dislocation (GND) density of GH3536-TL was calculated to be 8.29×10^{13}. This value is similar to the GND density of GH3536 (8.54×10^{13}) but much higher than that of GH3536-TH (4.53×10^{13}). This discrepancy may be attributed to the addition of TiC, which suppresses grain boundary migration and promotes recrystallisation, resulting in a lower GND density in GH3536-TH than in GH3536. The low energy density reduces the melt pool residence time, increases the cooling rate, and suppresses recrystallisation, leading to a significantly higher GND density in GH3536-TL than in GH3536-TH[46].

Phase identification of LPBF-fabricated specimens was conducted via XRD, with detailed analysis provided in the Supplementary Figure S3. XRD exhibits limitations in characterising nanoscale precipitates, however, TEM characterisation is thus performed (Figure 9) to clearly identify the phases formed in the LPBF-fabricated composites. Elliptical microscale particles (average equivalent diameter ∼3.5 μm) were found in the GH3536-TL specimen, which were confirmed to be Ti and C enrichment by the EDX mapping (Figures 9(a) and (b)). The selected area electron diffraction (SAED) patterns verified them to be TiC particles and they were very likely originating from the microscale TiC added to the GH3536. Also, the dispersed nanoscale particles and precipitates (Supplementary Figure S4(a)) with an average size of ∼80 nm were detected. In the high energy density specimen (GH3536-TH), the size of particles and precipitates increased to ∼250 nm (Supplementary Figure S4(b)). The TEM images indicated that the nanoscale particles were surrounded by dislocations (Figure 9(c)), suggesting the significant role of dislocation pining. For nanoscale TiC particles, distinct Ti and C enrichment was observed within near-spherical particles (Figure 9(c)). In contrast, Figure 9(e) showed enrichment of Ti, C, and Mo for the near-spherical precipitates and subgrain boundaries. Cr enrichment was also detected along subgrain boundaries, spatially distinct from Ti enrichment, and this is attributed to the $M_{23}C_6$ carbides in the GH3536 matrix, as evidenced by previous work[28]. Both the EDX mapping and SAED patterns (Figures 9(d) and (f)) confirmed the formation of nanoscale TiC particles and (Mo, Ti)C precipitates (MC carbides) in the composites. In summary, the added TiC particles exhibited hierarchical distribution in the GH3536

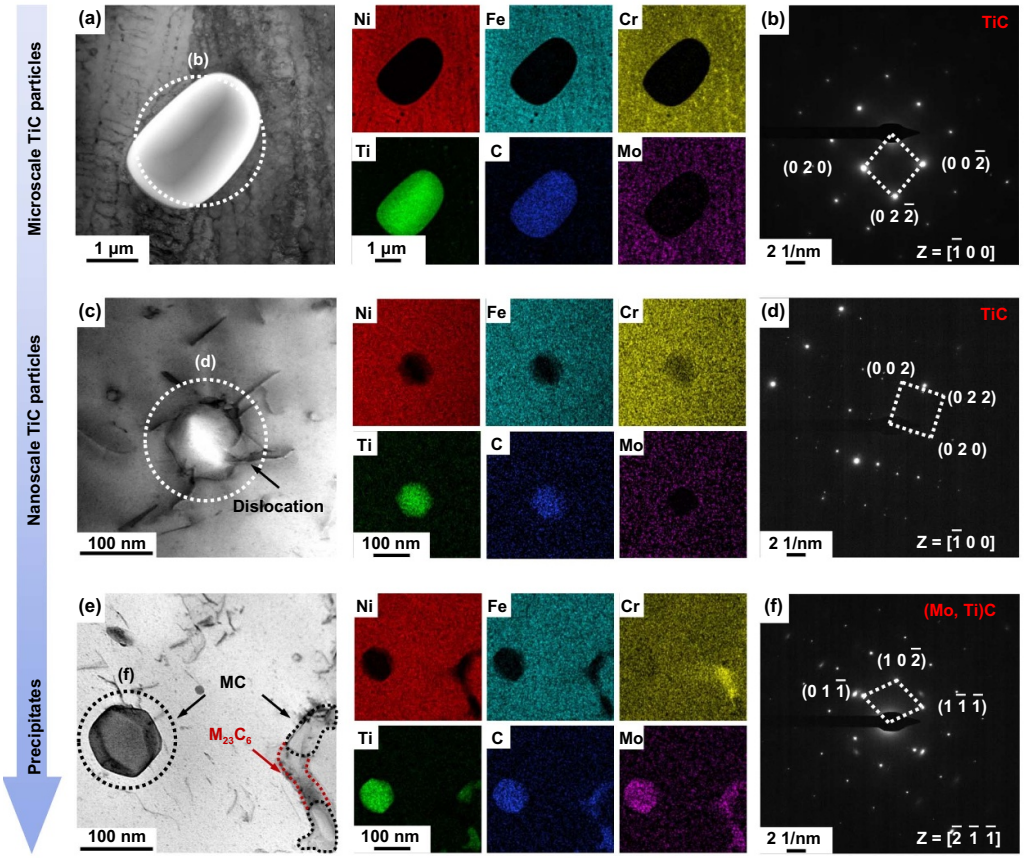

Figure 9. TEM characterisation of GH3536-TL specimen: (a) bright-field (BF) image and (b) SAED pattern of microscale TiC particles; (c) BF image and (d) SAED pattern of nanoscale TiC particles; (e) BF image and (f) SAED pattern of precipitates.

matrix, which was further discussed in the subsequent section (Section 4.3).

3.3. Tensile performance

Figure 10 and Table 6 show the tensile performance of the GH3536, GH3536-TH, and GH3536-TL specimens under both ambient (298 K) and elevated temperature (1 173 K) conditions. At ambient temperature, the ultimate tensile strength (UTS) of GH3536-TL reached 1 243 MPa that is 65% higher than GH3536 (755 MPa) and 6% higher than GH3536-TH (1 174 MPa). However, the elongation (EL) of the GH3536-TL specimen decreased to 5.4%, compared to 27.4% for GH3536. Although the addition of TiC greatly enhanced the ambient temperature UTS of the specimens, maintaining the strength-ductility balance remained challenging. The TEM characterisation of the fractured GH3536-TL specimen (Figures 10(c)–(f)) combined with the EDX mapping confirmed that both the TiC particles and (Mo, Ti)C carbides were surrounded by the dislocation pile-ups. These carbides acted as obstacles for dislocation motion, inducing localized bypassing and pile-ups mechanisms that could enhance the UTS. However, the resultant dislocation concentration may generate stress localization sites at the carbides' interfaces, contributing to a reduction in the ductility.

At elevated temperature, an EL of 42% was achieved in GH3536-TL, exhibiting a 238% enhancement compared to GH3536 (12%) and a 50% improvement relative to GH3536-TH (28%). Furthermore, the UTS of GH3536-TL was 304 MPa, higher than those of GH3536 (231 MPa) and GH3536-TH (301 MPa). The tensile test results showed that the UTS and EL of GH3536-TL at the elevated temperature were enhanced through the effect of adding TiC. The TEM characterisation of the fractured GH3536-TL specimen (Figures 10(e) and (f)) revealed distinct microstructural evolution. Compared to ambient condition (Figures 10(c) and (d)), the significantly reduced dislocation tangles have been detected, resulting from dynamic recovery and recrystallisation during the elevated temperature deformation. Notably, EDX mapping identified numerous near-spherical precipitates (~70 nm) enriched in Cr, Mo, and C, which were confirmed to be $M_{23}C_6$ carbides by the SAED examination (Figure 10(f)). This suggested the transformation occurred between the primary MC carbides and $M_{23}C_6$ during the 1 173 K tensile testing. The $M_{23}C_6$ formed continuous networks along subgrain boundaries in the GH3536-TL specimen during the tensile testing under the ambient condition, while most of the $M_{23}C_6$ carbides were still located at the subgrain boundaries (Figure 10(e)) with dislocations surrounding under the 1 173 K condition. This demonstrated that the grain boundary pinning caused by

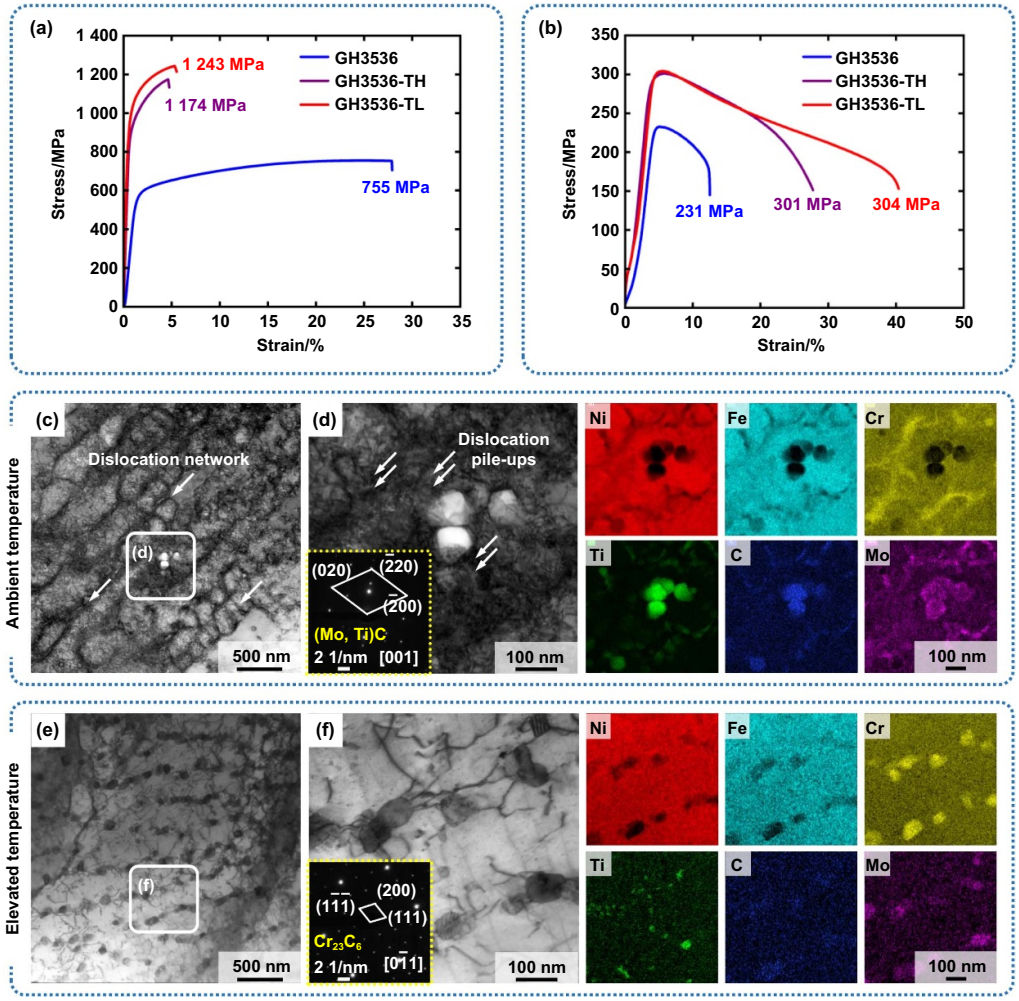

Figure 10. Tensile property analysis of GH3536, GH3536-TH, and GH3536-TL specimens: (a) engineering stress-strain curves at ambient temperature (298 K); (b) engineering stress-strain curves at elevated temperature (1 173 K); (c) and (d) BF TEM images and EDX mapping of GH3536-TL specimen after 298 K tensile tests; (e) and (f) BF TEM images and EDX mapping of GH3536-TL specimen after 1 173 K tensile tests; the insets in (d) and (f) are SAED patterns.

Table 6. Tensile properties of GH3536, GH3536-TH, and GH3536-TL specimens.

	Ambient temperature (298 K)		Elevated temperature (1 173 K)	
Specimens	UTS/MPa	EL/%	UTS/MPa	EL/%
GH3536	755 ± 5	27 ± 2	231 ± 4	12 ± 2
GH3536-TH	1 174 ± 5	5 ± 0.3	301 ± 3	28 ± 4
GH3536-TL	1 243 ± 4	5 ± 0.2	304 ± 5	42 ± 3

the $M_{23}C_6$ carbides played a key role in enhancing the material's ductility under the elevated-temperature tensile testing.

4. Discussions

4.1. Simulation of melt pool dynamics and multiscale evolution of TiC particles

To investigate the evolution pathways of TiC particles, CFD simulations of the melt pool were performed. The comparison between the simulated (SIM) single-track melt pool geometry and the experimentally (EXP) measured melt pools was analysed to validate the model reliability and accuracy. It was found that for the GH3536-TH specimen, the SIM melt pool dimensions included a width of 128 μm and depth of 41 μm, compared to the EXP of 143 μm (width) and 49 μm (depth), offering errors of 11% and 16%, respectively (Figure 11(a)). The SIM predicted GH3536-TL specimen dimensions included a width of 82 μm and depth of 29 μm, compared to EXP values of 91 μm (width) and 32 μm (depth), offering relative errors of 10% and 9%, respectively (Figure 11(b)). Overall, the simulation results demonstrated

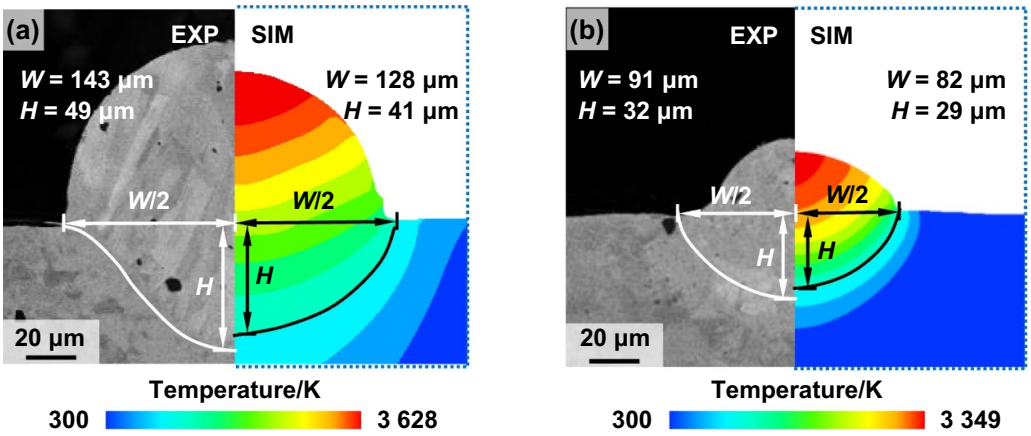

Figure 11. Comparison between the simulated single-track melt pool geometry and the experimental melt pools: (a) GH3536-TH; (b) GH3536-TL.

satisfactory agreement with experimental measurements and the deviations may be attributed to the randomness of the initial powder used.

Figure 12 illustrates the temperature field of single-track melt pools in GH3536-TH and GH3536-TL, along with the particle dispersion characteristics following solidification. The peak temperatures of GH3536-TH reached 3 628 K, which is 279 K higher than that of GH3536-TL. The melt pool surface morphology exhibited comparatively rougher characteristics relative to GH3536-TH. Fixed-point temperature monitoring (AH/AL: melt pool centre; BH/BL: melt pool edge) in Figures 12(a-i) and (b-i) quantifies the thermodynamic variations between GH3536-TH and GH3536-TL. The temporal changes of temperature at two selected measurement points are shown in Figures 12(a-iv) and (b-iv). In the GH3536-TH specimen, the melt pool required 0.26 ms to reach the peak temperature of 3 628 K, which was notably longer than the 0.12 ms required for GH3536-TL. Notably, while peak temperatures in both specimens exceeded the melting point of TiC (3 300 K), the time spent at temperatures above 3 300 K in the GH3536-TL melt pool was reduced by over 50% (0.08 ms vs. 0.19 ms).

Two temporal intervals (0.16–0.22 ms and 0.76–0.82 ms for GH3536-TH; 0.08–0.14 ms and 0.38–0.44 ms for GH3536-TL, see Figures 12(a-iii) and (b-iii)) at identical spatial positions within the melt pool were selected for simulating melt pool behaviour. Figure 13 demonstrates the multiscale evolution patterns of TiC particles in both GH3536-TH and GH3536-TL. As shown in Figure 13(a), the melt pool temperature in GH3536-TH was rapidly elevated to 3 628 K, which induced vigorous fluid flow dynamics. Rapid thermal excitation created substantial velocity gradients in TiC particles, with instantaneous velocity vectors reaching 1.89 $m{\cdot}s^{-1}$ directed towards the pool base (Figure 13(a-i)). The black dashed markers indicated that TiC particles at the laser irradiation centre underwent preferential melting and morphological transformation into irregular polyhedra with coarse edges (Figure 13(a-ii)).

The evolution of TiC particles in the melt pool is governed by two competing mechanisms: Marangoni flow (indicated by black velocity vectors) from thermal gradients and vaporisation-induced recoil pressure[47]. Particle coarsening was induced by the interaction between the two mechanisms at 0.20 ms. The morphological transformation of TiC was subsequently accelerated through continuous laser irradiation. TiC particles with an isosceles triangular morphology were transformed into equilateral triangular shapes. Ultimately, irregular polyhedral TiC structures were generated through surface tension-driven mechanisms and rapid solidification of the melt pool (Figure 12(a-iii)). The spattering exhibited anisotropic characteristics: as shown in Figure 13(a), spatter from the powder bed (within purple dashed lines) occurred perpendicular to the scanning direction (X-axis), while TiC particle spatter (within red circles) aligned along the X-axis with an initial velocity of 1.2 $m{\cdot}s^{-1}$.

As shown in Figure 13(b), two critical differences in the behaviour simulation of the GH3536-TL melt pool and that of the GH3536-TH melt pool were observed. On the one hand, the velocity of TiC particles was reduced from 1.89 $m{\cdot}s^{-1}$ to 1.76 $m{\cdot}s^{-1}$ due to decreased thermal gradients. On the other hand, partial melting of TiC particles was observed, accompanied by weakened coarsening effects (within the black dashed lines). This phenomenon resulted in significant differences in the final size distribution and population density of TiC particles in the two energy density conditions. Both differential phenomena were confirmed through statistical results in Figure 4(e). Experimental results revealed that the GH3536-TL specimen had a smaller average particle size but a higher particle number than GH3536-TH.

Figure 13(c) shows the evolution of TiC particles during the period of 0.76–0.82 ms in GH3536-TH. Enhanced spattering and coarsening phenomena were observed compared to GH3536-TL. Notably, all ejected TiC particles spatter maintained spherical morphologies consistent with the initial powder characteristics. The premature spattering phenomenon of TiC particles prior to the coarsening stage may

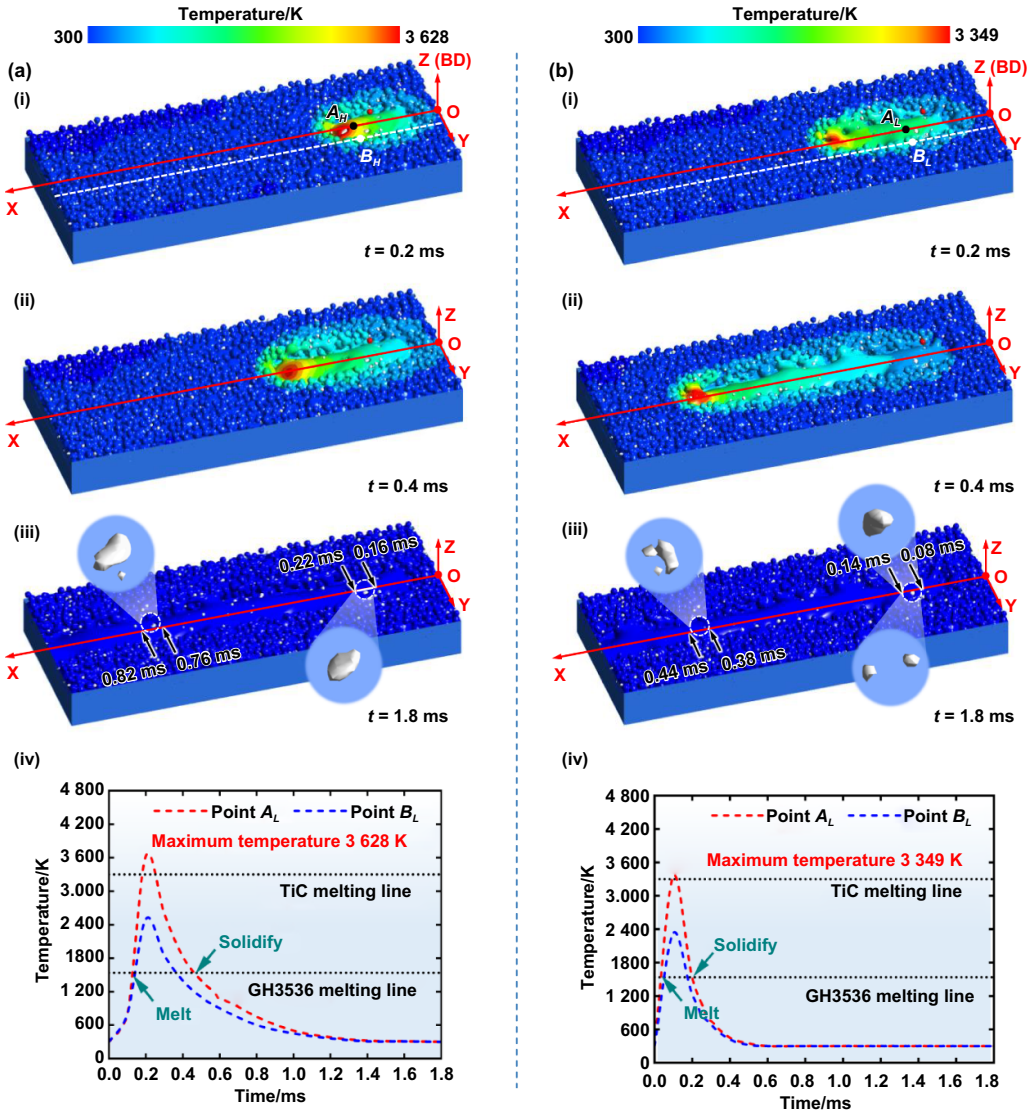

Figure 12. Temperature fields and solidified particle distribution characteristics at different stages: (a) GH3536-TH: (a-i) and (a-ii) transient temperature profiles within the melt pool, (a-iii) particle dispersion in the solidified pool, (a-iv) thermal histories at two monitoring points in the melt pool; (b) GH3536-TL: (b-i) and (b-ii) transient temperature profiles within the melt pool, (b-iii) particle dispersion in the solidified pool, (b-iv) thermal histories at two monitoring points in the melt pool.

be confirmed. Figure 13(d) presents the melt pool behaviour simulation results for GH3536-TL at the same powder bed locations in Figure 13(c). The simulation results indicate that the particle coarsening phenomenon remains insignificant. Under low energy density conditions, TiC particle spattering is effectively suppressed, with most particles remaining retained within the melt pool. This difference arises from the change in the physical field of the melt pool. The thermal gradient within the melt pool is reduced due to decreased energy density, leading to a diminished surface tension gradient. This attenuation phenomenon results in a deceleration of the Marangoni convection velocity. At the same time, low energy input leads to a decrease in the metal vapor recoil pressure and the evaporation rate of the melt pool, thereby reducing the shear force on the melt pool surface. The dynamic response of the melt pool and the kinetic energy of TiC particles are diminished due to reduced energy density. This mechanism was quantitatively validated through velocity measurements of TiC particles. A decrease from 1.59 $m{\cdot}s^{-1}$ to 1.43 $m{\cdot}s^{-1}$ was observed. This kinetic energy reduction explains the increased TiC particle loss at high energy densities (see Section 3.1).

4.2. Coarsening mechanisms of TiC

The coarsening of TiC particles is governed by two competing mechanisms during the LPBF process: mechanical impingement and chemical transport[25]. The coupled interactions between melt pool dynamics and particle evolution were quantitatively analysed through computational evaluation of multiphysics dimensionless quantities, including the Reynolds (R_e), Peclet (P_e), separation (S_e), buoyancy (B_o), and Stokes (S_{tk}) numbers.

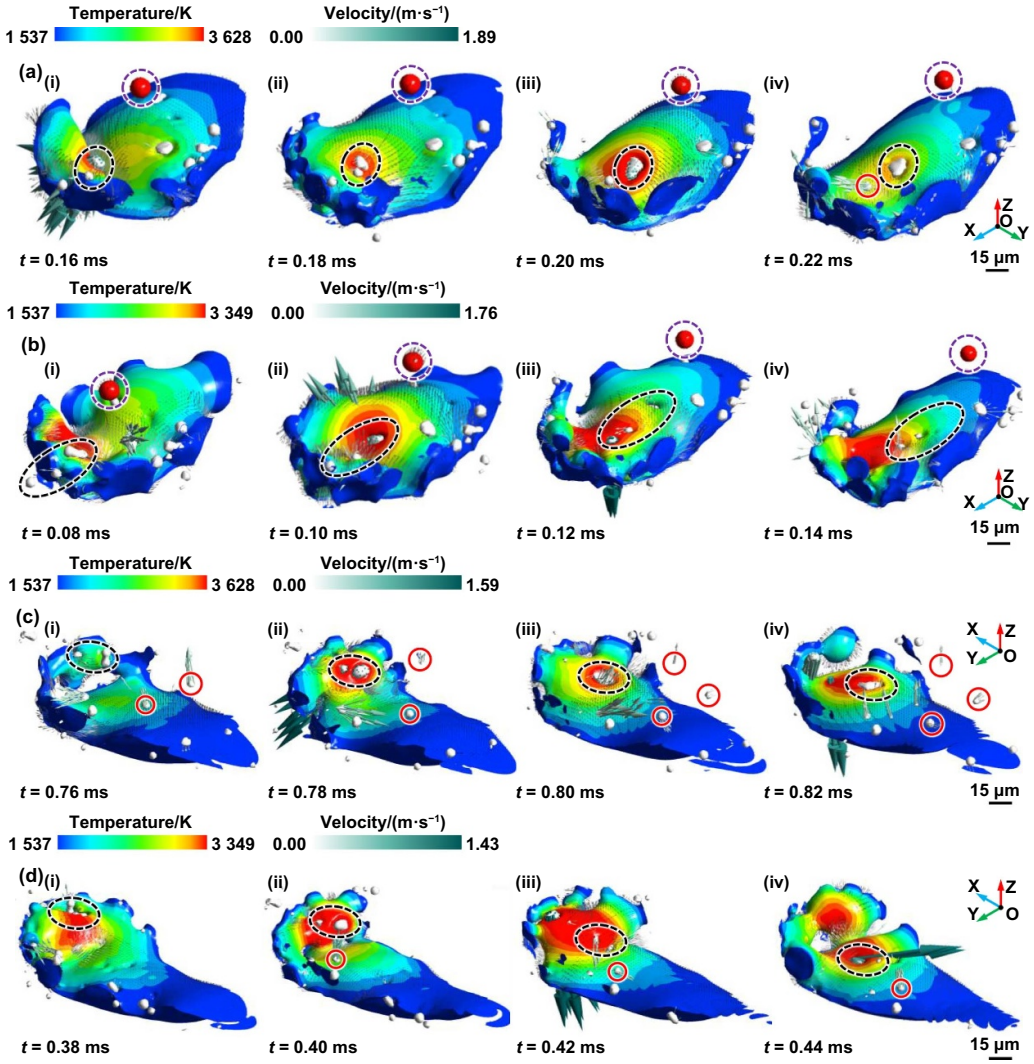

Figure 13. Simulation results of the melt pool behaviour and TiC particle evolution at the same powder bed location: (a) temperature and velocity fields within the GH3536-TH melt pool during the 0.16–0.22 ms interval; (b) temperature and velocity fields within the GH3536-TL melt pool during the 0.08–0.14 ms interval; (c) temperature and velocity fields in the GH3536-TH melt pool during the 0.76–0.82 ms interval; (d) temperature and velocity fields in the GH3536-TL melt pool during the 0.38–0.44 ms interval. The black dashed lines denote TiC particles within the melt pool, the purple dashed lines indicate melt spatter, and the red circles highlight TiC particle spatter.

R_e was employed to characterise the flow behaviour of melt metal around TiC particles within the melt pool[25]:

$$R_e = \frac{\rho_p \nu L}{\mu} \tag{9}$$

$$\nu = \frac{(T_m - T_b)\,\sigma_c H}{4\mu L} \tag{10}$$

where v is the fluid velocity, ρ_P is the GH3536 alloy density, L is the melt pool length, μ is the dynamic viscosity, T_m is the melting temperature, T_b is the vaporisation temperature, σ_c is the surface tension coefficient, and H is the melt pool depth. The present calculation is actually based on both the melt pool simulation and the non-equilibrium solidification calculation by using the Thermo-Calc software (Table 3). For the GH3536-TH, the fluid velocity (v) is 6.17 m·s^{-1}, the melt pool length (L) is 290 μm, and the melt pool depth (H) is 41 μm. For the GH3536-TL, the fluid velocity (v) is 2.62 m·s^{-1}, the melt pool length (L) is 200 μm, and the melt pool depth (H) is 29 μm.

The R_e values for GH3536-TH and GH3536-TL melt pool were calculated as 1 486.38 and 915.29, respectively. A laminar flow regime was confirmed in both melt pools. However, the motion of TiC particles within the molten pools cannot be precisely determined due to surface wettability effects. The relative velocity between TiC particles and melt was quantified through V_{rel}[48]:

$$\nu_{rel} = \frac{(\rho_p - \rho_{TiC})\,\nu}{9\mu t} n^2 \tag{11}$$

where ρ_{TiC} is the TiC density, t is the residence time of a fluid element (∼100 μs for LPBF), and n is the particle diameter.

As shown in Figure 14, the computational analysis of the variation of R_e with TiC particle diameter (n) demonstrated

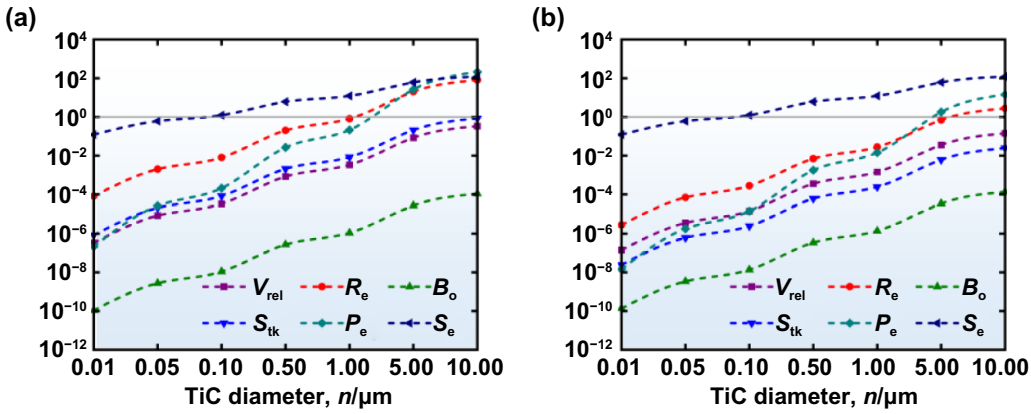

Figure 14. The relationship between dimensionless quantities and TiC particle diameter (n) in melt pool dynamics calculations: (a) the various dimensionless numbers in the GH3536-TH melt pool; (b) the various dimensionless numbers in the GH3536-TL melt pool.

distinct flow regimes. In GH3536-TH, TiC particles with diameters below 1.5 μm exhibited local $R_e < 1$. This value indicates viscosity-dominated flow and a stable laminar boundary layer around the TiC particles. This viscous suppression of inertial effects likely reduces particle impingement frequency, thereby limiting coarsening. Conversely, particles exceeding 1.5 μm diameter induced localised turbulent fluctuations ($R_e > 1$). In GH3536-TL, TiC particles with diameters below 5.5 μm were calculated to exhibit $R_e < 1$. This observation indicated that viscous effects dominated the flow around relatively large particles. The critical particle size for flow regime transition was found to be controlled by energy density.

To analyse particle coarsening mechanisms induced by interparticle impingement, B_o and S_{tk} were calculated[25]:

$$B_0 = \frac{4(\rho_p - \rho_{TiC})gt}{27\mu H}n^2 \tag{12}$$

$$S_{tk} = \frac{(\rho_p - \rho_{TiC})\nu}{18\mu L}n^2. \tag{13}$$

Numerical analysis revealed that the B_o value of TiC particles under both energy density conditions was substantially less than unity ($B_o \ll 1$). This indicated negligible buoyancy effects in the melt pool, where particle dispersion was primarily governed by fluid flow and diffusion mechanisms. The nonuniform TiC dispersion observed in SEM images (Figure 5) likely originates from this flow-dominated transport regime. In GH3536-TL, nanoscale TiC particles exhibited viscosity-dominated transport within the melt pool, where viscous forces governed particle motion. The distinct cooling rates under different energy densities resulted in contrasting TiC dispersion patterns. Significant differences in S_{tk} were observed between energy conditions. In GH3536-TH, TiC particles with diameters of 5 μm (as added in this study) were calculated to exhibit an S_{tk} of 0.23. This value was reduced to 0.006 in GH3536-TL. The S_{tk} difference reveals distinct transport mechanisms of TiC particles within melt pools. Increased S_{tk} values in GH3536-TH indicate enhanced inertial effects, which promote particle impingement and coarsening.

To investigate the competitive influence of convective and diffusive transport mechanisms in melt pools under varying energy densities, P_e and S_e were computationally analysed[25]:

$$P_e = \frac{V_{rel}}{2d_{TiC}}n \tag{14}$$

$$S_e = \frac{1}{4\sqrt{d_{TiC}t^3}\sqrt{V_{TiC}}}n \tag{15}$$

where V_{TiC} is the TiC molar volume and d_{TiC} is the TiC diffusion coefficient.

Computational results demonstrate that TiC particles with diameters less than 2 μm exhibit $P_e < 1$ (with $P_e \ll 1$ for $n < 500$ nm) in GH3536-TH. This indicates that heat and mass transfer around submicron TiC particles predominantly occurs through chemical transport rather than convective fluid motion during LPBF. Convective effects become significant for TiC diameter $n > 2$ μm, increasing the impingement-induced coarsening possibility. Conversely, in GH3536-TL, chemical transport dominates across a broader size range ($P_e < 1$ for $n < 4.5$ μm, with $P_e \ll 1$ for $n < 1$ μm). This indicates that the chemical transport mechanism affects TiC particles of a larger size range.

$S_e < 1$ at two energy densities indicates synchronised flow between the TiC particles and GH3536, specifically for nanoscale TiC particles (<100 nm). Interparticle impingement between TiC particles were effectively suppressed. Consequently, localised chemical transport was generated between adjacent nanoscale TiC particles. Cooling time of the melt pool was prolonged under high energy density conditions. This chemical transport-driven growth mechanism was amplified. The size variation phenomenon observed in TiC particles (Figure 5) was thereby explained.

Figure 14 illustrates the relationship between dimensionless quantities and TiC particle diameters. Nanoscale

(<100 nm) and microscale (>1 μm) particles exhibit fundamentally different coarsening pathways. For nanoscale TiC particles under both energy densities, particle motion was dominated by viscous forces ($S_{tk} < 0.01$). Impingement-driven coarsening was suppressed, with coarsening primarily occurring through chemical transport mechanisms. In contrast, microscale TiC primarily underwent impingement-dominated coarsening. Comparative analysis of dimensionless quantities reveals distinct particle behaviour under different energy densities. On the one hand, $R_e > 1$ corresponded to TiC diameters larger than 1.5 μm under high energy conditions, whereas this threshold increases to 5.5 μm under low energy input. Under high energy density conditions, TiC particles with diameters exceeding 2 μm were found to exhibit $P_e > 1$. In contrast, $P_e > 1$ was only observed in TiC particles larger than 4.5 μm under low energy density conditions. Elevated S_{tk} observed at higher energy densities demonstrates enhanced inertial effects. The combined influence of these factors significantly enhances impingement-driven coarsening events between TiC particles within the high energy density melt pool. Furthermore, TiC particle growth may be accelerated through concurrent chemical transport and impingement-driven mechanisms. This phenomenon is primarily attributed to the instability and the extended cooling time at high energy density melt pools. This finding provides a unified explanation for both the TiC coarsening behaviour predicted by melt pool simulations (Section 4.1) and the microstructural features observed via SEM (see Section 3.1).

4.3. Hierarchical distribution of TiC particles

As shown in Figure 15, the TiC particles within the GH3536 demonstrate a multiscale structural transition pattern and hierarchical distribution.

First level distribution: microscale TiC particles with irregular polyhedral morphologies show uniform dispersion in both GH3536-TH and GH3536-TL (Figure 3). Partial coarsening occurs via impingement mechanisms and the irregular polyhedral shape can be remained under the rapid solidification within the melt pools. The high melting point of TiC (3 300 K) enables the survival of unmelted particles within the matrix.

Second level distribution: a significant number of submicron and nanoscale TiC particles (approximately 250 nm and 80 nm in size) were found dispersed in GH3536-TH and GH3536-TL. The Gaussian laser beam irradiation likely induces TiC particles into submicron and nanoscale fragments through thermal shock mechanisms. TiC particles melt at the edges and quickly shrink into near-spherical shapes under the influence of surface tension[49]. Subsequent growth of these particles occurs via chemical transport mechanisms, where viscous forces govern the melt flow around particles. During dendrite growth, some TiC particles were engulfed into the dendrite structure, while others were entrapped between the dendrites (Figure 5). Subsequently, these particles were fully melted.

Third level distribution: despite the low initial concentrations of Ti (0.01 wt%) and C (0.07 wt%) in the GH3536 alloy, significant precipitation of Mo/Ti-enriched MC carbides was observed in both GH3536-TL and GH3536-TH. It can be inferred that TiC particles were melted and decomposed under Gaussian laser irradiation. The C and Ti atoms react with Mo from GH3536 to form (Mo, Ti)C carbides. The MC carbides are present in the following forms: (1) near-spherical precipitates within subgrains, approximately 250 nm and 80 nm in size; (2) continuous precipitates between the dendrites; (3) discontinuous precipitates between the dendrites (Figure 6).

Fourth level distribution: it is well-known that spattering is inevitable during the LPBF process[50]. The spattering phenomenon of TiC particles was observed through the melt pool simulation. Furthermore, TiC particle spattering occurred before the particle coarsening (Section 4.1), which will be further investigated in future studies.

4.4. The high ductility of LPBF-fabricated composites

In this study, the low energy density specimen (GH3536-TL) demonstrates significantly enhanced ductility (Figures 10(a) and (b)). This enhanced ductility arises from the transformation of carbides (MC to $M_{23}C_6$) together with a bimodal grain distribution.

The phase transitions of the precipitates during the elevated-temperature tensile testing could significantly influence the mechanical performance. Previous studies revealed that the stress concentrations induced by coarsened $M_{23}C_6$ carbides along grain boundaries at 1 173 K contributed to the reduction in the elevated-temperature ductility in GH3536 alloy[51,52]. In the present study, MC carbides exhibited thermal instability below 1 173 K, as confirmed by[53], while the elemental diffusion at elevated temperatures promoted the combination between C and Cr/Mo elements, forming near-spherical $M_{23}C_6$ carbides along subgrain boundaries (Figures 10(e) and (f)). These carbides could pin the dislocations and stabilise grain boundaries, thereby improving the elevated-temperature ductility of GH3536-TL specimens by restricting grain boundaries migration.

Under high energy density conditions, TiC particles and other precipitates get coarsen, intensifying stress concentrations around particles and carbides. In contrast, finer TiC and precipitates promote more tortuous crack paths. This distinction helps explain the lower elevated temperature ductility of GH3536-TH (28%) compared with GH3536-TL (42%). The nanoscale TiC alters the solidification behaviour of the melt pool, further reducing the temperature gradient and solidification rate[54], lowering the texture strength and generates fine-grained regions (Figure 7(c-i)). In the bimodal grain structure, the CG and FG regions have different dislocation storage capacities, resulting in strain incompatibility. The CG region generates a significant amount of GND, inducing heterogeneous deformation-induced (HDI) strengthening, thereby improving tensile strength[55]. GND accumulation establishes back stress fields oriented towards grain interiors. During the initial elastic stage of tensile deformation, both CG and FG regions maintain elastic responses. Upon entering the plastic stage, CG regions preferentially initiate plastic deformation, while FG regions retain elastic constraints[56]. This mechanical incompatibility

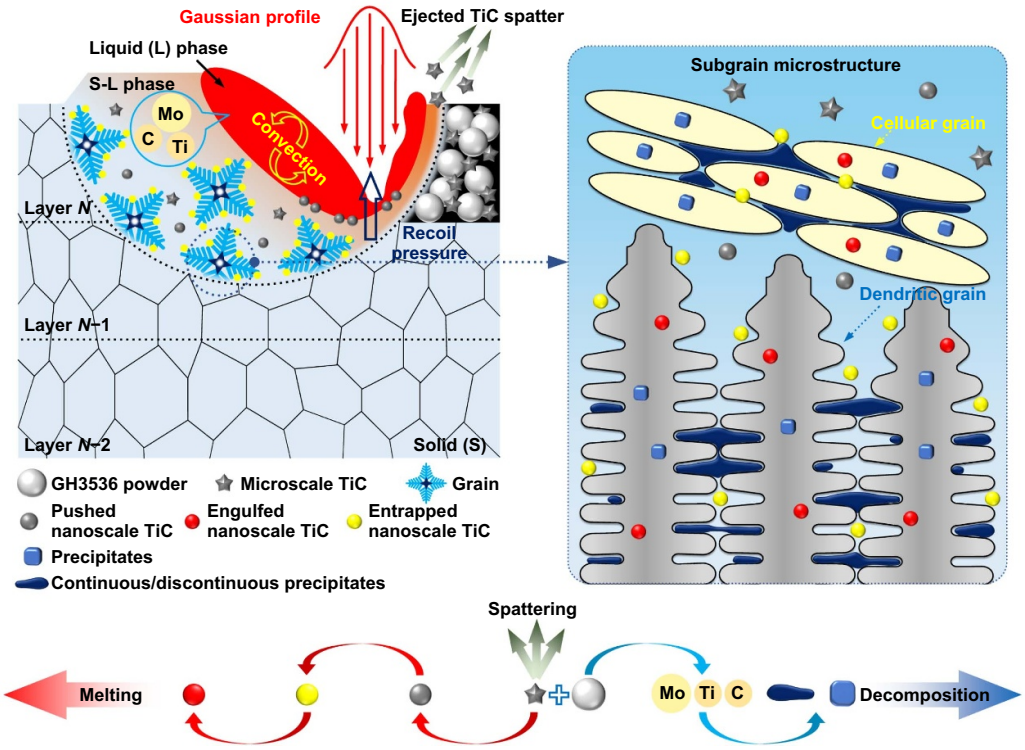

Figure 15. Schematic of multiscale evolution of TiC particles.

induces progressive accumulation of back stress to equilibrate external loading. The back stress delays plastic yielding in the FG regions and also enhances the overall ductility through stress redistribution mechanisms[57].

At ambient conditions, TiC particles and MC carbides significantly enhance the UTS (1 243 MPa) of GH3536-TL specimens through dislocation pile-ups (Figure 10(d)), as confirmed by[58,59]. However, stress concentrations around these particles and carbides may cause a strength-ductility imbalance; the continuously distributed MC carbides along subgrain boundaries act as preferred crack initiation sites and promote premature fracture. In addition, the stress concentration sites near TiC particles suppresses full activation of HDI strengthening mechanisms, such as stress redistribution via the back stress. This restricts the participation of FG regions during the plastic deformation, further weakening the ductility enhancement effects.

5. Conclusions

In this study, the TiC particle evolution mechanism under different energy densities was investigated. The main conclusions are presented below.

(1) A 72% reduction in TiC particle number and a particle size increase from 3.55 μm to 3.98 μm were observed as energy density increased from 45 J·mm^{-3} to 143 J·mm^{-3}. Numerical simulations attribute this to multiparticle cooperative coarsening and enhanced particle spattering under high energy density. Further analysis using dimensionless quantities, such as R_e, P_e, and S_{tk}, reveals that the coarsening of nanoscale TiC (<100 nm) is primarily governed by chemical transport, while the coarsening of microscale TiC (3–7 μm) is dominated by impingement. The critical threshold of TiC diameter for impingement-driven growth reduced under high energy density conditions, resulting in amplified impingement-driven coarsening.

(2) TiC particles exhibit four-tiered composed hierarchical distribution characteristics in LPBF-fabricated specimens. In the first level, irregular microscale TiC undergoes controlled growth through the impingement-driven coarsening mechanism. In the second level, submicron and nanoscale TiC particles are engulfed into the dendrite structure, while others are entrapped between the dendrites. In the third level, partial dissolution of TiC particles occurs under laser irradiation, leading to the formation of (Mo, Ti)C carbides, including both continuous and discontinuous precipitates between dendrites, as well as near-spherical nanoprecipitates within subgrains. In the fourth level, particle spattering occurs within the TiC particles evolution, as validated by the melt pool simulations.

(3) The low energy density specimen (GH3536-TL) developed near equiaxed grain structures with an average size of 10.69 μm. At ambient temperature, GH3536-TL exhibited an exceptional UTS of 1 243 MPa, representing a 65% enhancement compared to GH3536. Remarkable strength-ductility synergy was achieved at 1 173 K, with GH3536-TL demonstrating a UTS value of 304 MPa and EL of 42%, which were 32% and 238% higher than those

of GH3536, respectively. The ductility enhancement is mainly attributed to the coordinated effects of bimodal grain structures and the transformation of carbides (MC to $M_{23}C_6$).

Acknowledgments

The authors appreciate the financial support from the Shandong Provincial Natural Science Foundation (Grant Nos. ZR2023YQ053, ZR2022ZD08, and ZR2023QE287).

CRediT authorship contribution statement

Peng Zhao: writing—original draft, methodology, investigation. **Quanquan Han:** funding acquisition, conceptualization. **Zhenhua Zhang:** validation, investigation. **Zhongyang Sui:** visualization, software. **Liqiao Wang:** writing—review & editing. **Bo Song:** visualization, resources. **Min Zhu:** investigation. **Xiebin Wang:** conceptualization. **Rossitza Setchi:** methodology. **Chuanzhen Huang:** resources.

ORCID iDs

Quanquan Han 0000-0002-0657-9901
Bo Song 0000-0002-6730-3917
Xiebin Wang 0000-0001-5132-6797

References

[1] Chen L Y, Qin P, Zhang L N and Zhang L C. 2024. An overview of additively manufactured metal matrix composites: preparation, performance, and challenge. *Int. J. Extrem. Manuf.* **6**, 052006.
[2] Tekoğlu E et al. 2024. Metal matrix composite with superior ductility at 800 °C: 3D printed In718+ZrB_2 by laser powder bed fusion. *Composites B* **268**, 111052.
[3] Chen L Y, Liang S X, Liu Y J and Zhang L C. 2021. Additive manufacturing of metallic lattice structures: unconstrained design, accurate fabrication, fascinated performances, and challenges. *Mater. Sci. Eng. R* **146**, 100648.
[4] Chu Y-H, Chen L-Y, Qin B-Y, Gao W B, Shang F M, Yang H-Y, Zhang L N, Qin P and Zhang L-C. 2024. Unveiling the contribution of lactic acid to the passivation behavior of Ti–6Al–4V fabricated by laser powder bed fusion in hank's solution. *Acta Metall. Sin.* **37**, 102–118.
[5] Zhang Y-F, Chen L-Y, Liu Y, Yang H-Y, Peng J-H, Zheng C B, Zhang L N and Zhang L-C. 2025. Corrosion behavior of NiTi alloys fabricated by laser powder bed fusion in relation to the formed passive films in Hank's solution. *J. Mater. Res. Technol.* **34**, 1933–1946.
[6] Tekoglu E et al. 2024. Superior high-temperature mechanical properties and microstructural features of LPBF-printed In625-based metal matrix composites. *Mater. Today* **80**, 297–307.
[7] Cheng X P, Guo Q Y, Liu C X and Ma Z Q. 2025. Simultaneous enhancement of elevated temperature strength and ductility in additive-manufactured nickel-based superalloy via doping Y_2O_3 nanoparticles. *J. Mater. Sci. Technol.* **210**, 312–324.
[8] Zhang X G, Zhai W G, Liu Y J, Zhou W, Chen Y, He C, Zhang H, Wang C, Wang Q Y and Liu F L. 2025. Temperature-dependent mechanical properties of La_2O_3-reinforced 316L stainless steel fabricated by laser powder bed fusion. *Mater. Sci. Eng. A* **925**, 147884.
[9] Wang S D, Zhao Y F, Wen P Y, Yang Z G, Sha G, Wang W, Jiao Z B, Kim H S and Chen H. 2025. Precipitate evolution in an ultrahigh-strength, carbon-impurity-enhanced maraging steel manufactured via laser powder bed fusion. *Acta Mater.* **300**, 121455.
[10] Snopiński P, Kotoul M, Petruška J, Rusz S, Żaba K and Hilšer O. 2023. Revealing the strengthening contribution of stacking faults, dislocations and grain boundaries in severely deformed LPBF AlSi10Mg alloy. *Sci. Rep.* **13**, 16166.
[11] Liu W J, Li H, Yin Q X and Zhou X. 2025. Promoting densification and strengthening effect of ultrasonic impact treatment on Haynes 230 alloy manufactured by laser powder bed fusion. *J. Mater. Sci. Technol.* **216**, 226–240.
[12] Ma X F, Wang C, Li R H, Duan J J, Cao M X, Luo J L, Zou X D, Shao L Y and Pan L L. 2025. Tailoring microstructure and oxidation resistance in directed energy deposited Inconel 625 alloy by the addition of submicron-ZrC particles. *Mater. Charact.* **224**, 115017.
[13] Yuan Z W, Chang F C, Chen A Z, Li F G, Ma R, Bai J and Zheng J C. 2022. Microstructure and properties of SLM-Hastelloy X alloy after different hot isostatic pressing + heat treatment. *Mater. Sci. Eng. A* **852**, 143714.
[14] Zhang Z H, Han Q Q, Liu Z Y, Wang L Q, Zhang H, Zhao P, Zhu G L, Huang C Z and Setchi R. 2023. Cracking behaviour and its suppression mechanisms with TiB_2 additions in the laser additive manufacturing of solid-solution-strengthened Ni-based alloys. *Composites B* **266**, 111023.
[15] Ma J, Niu J Z, Lin Y, Zhang X Z and Jin F. 2024. Laser powder bed fusion of CoCrNi composite with high fraction of TiC: the microstructure and mechanical properties at different temperatures. *Mater. Sci. Eng. A* **911**, 146929.
[16] Jia L, Yi H, Jiao F R and Cao H J. 2025. Particle floating and transfer effect in cored wire arc additive manufacturing: formation mechanism and laser shock inhibition. *Int. J. Mach. Tools Manuf.* **207**, 104260.
[17] Zhang Y M, Yu Y F, Wang L, Li Y, Lin F and Yan W T. 2022. Dispersion of reinforcing micro-particles in the powder bed fusion additive manufacturing of metal matrix composites. *Acta Mater.* **235**, 118086.
[18] Wang G, Zhang Y M, Zou B K, Liu Y, Zheng S Q, Li X C, Yan W T, Li Z and Wang Y M. 2023. Enhanced plasticity due to melt pool flow induced uniform dispersion of reinforcing particles in additively manufactured metallic composites. *Int. J. Plast.* **164**, 103591.
[19] Wang L, Guo Q L, Chen L Y and Yan W T. 2023. In-situ experimental and high-fidelity modeling tools to advance understanding of metal additive manufacturing. *Int. J. Mach. Tools Manuf.* **193**, 104077
[20] Wang L, Guo Z X, Peng G C, Wu S W, Zhang Y M and Yan W T. 2024. Evaporation-Induced Composition Evolution in Metal Additive Manufacturing. *Adv. Funct. Mater.* **35**, 2412071.
[21] Qu M L, Yuan J D, Nabaa A L, Huang J Y, Chuang C A and Chen L Y. 2024. Melting and solidification dynamics during laser melting of reaction-based metal matrix composites uncovered by in-situ synchrotron X-ray diffraction. *Acta Mater.* **271**, 119875.
[22] Rees D T, Leung C L A, Elambasseril J, Marussi S, Shah S, Marathe S, Brandt M, Easton M and Lee P D. 2023. In situ X-ray imaging of hot cracking and porosity during LPBF of Al-2139 with TiB_2 additions and varied process parameters. *Mater. Des.* **231**, 112031.

[23] Guo D, Lambert-Garcia R, Hocine S, Fan X Q, Greenhalgh H, Shahani R, Majkut M, Rack A, Lee P D and Leung C L A. 2024. Correlative spatter and vapour depression dynamics during laser powder bed fusion of an Al-Fe-Zr alloy. *Int. J. Extrem. Manuf.* **6**, 055601.
[24] Ren Z S, Gao L, Clark S J, Fezzaa K, Shevchenko P, Choi A, Everhart W, Rollett A D, Chen L Y and Sun T. 2023. Machine learning–aided real-time detection of keyhole pore generation in laser powder bed fusion. *Science* **379**, 89–94.
[25] Hou W Y, Stubbs T, Lisa D S, Chang Y T, Charpagne M A, Smith T M, Huang A J and Cordero Z C. 2024. Dissolution zone model of the oxide structure in additively manufactured dispersion-strengthened alloys. *Addit. Manuf.* **96**, 104554.
[26] Zhai W G, Zhou W, Yu Y and Nai S M L. 2024. Direct evidence of melting and decomposition of TiC particles in laser powder bed fusion processed 316L-TiC composite. *J. Mater. Sci. Technol.* **198**, 166–175.
[27] Gao S B et al. 2023. Additive manufacturing of alloys with programmable microstructure and properties. *Nat. Commun.* **14**, 6752.
[28] Zhang Z H, Han Q Q, Yang S Z, Yin Y Y, Gao J and Setchi R. 2021. Laser powder bed fusion of advanced submicrometer TiB_2 reinforced high-performance Ni-based composite. *Mater. Sci. Eng. A* **817**, 141416.
[29] Liang Y Z, Han Q, Sui Z, Zhang Z, Zhang H, Gu H, Wu D, Wang L, Liu H and Setchi R. 2025. Laser powder bed fusion of high-strength crack-free Al7075 alloy with the in-situ formation of TiB_2/Al_3Ti-reinforced phases and nucleation agents. *Composites B* **289**, 111940.
[30] Kim J and Kang S. 2012. Elastic and thermo-physical properties of TiC, TiN, and their intermediate composition alloys using ab initio calculations. *J. Alloys Compd.* **528**, 20–27.
[31] Wang Y Q, Zhou X M, Xiong X C, Yuan Y L, Bai X W, Fu J J and Wu H H. 2025. Numerical simulation of heat and mass transfer in wire arc additive manufacturing of TiC particle reinforced 6061 aluminum alloy. *Int. Commun. Heat Mass Transf.* **161**, 108454.
[32] Liang Y R, Jiao H, Yang W D, Feng J W, Wang Q X and Zhao K. 2025. TiC_w/TiC ceramics composites: SPS preparation, thermal and mechanical properties. *Mater. Sci. Eng. B* **314**, 118005.
[33] Wang Q, Chen L and Liang C P. 2025. Effects of alloying elements on the solubility, diffusivity, and permeability of hydrogen in TiC from first-principles calculation. *Nucl. Mater. Energy* **43**, 101924.
[34] Zhang Y M, Wu S W, Guo Z X, Peng G C, Wang L and Yan W T. 2025. Defects caused by powder spattering and entrainment in laser powder bed fusion process: high-fidelity modeling of gas, melt pool and powder dynamics. *Acta Mater.* **288**, 120816.
[35] Hirt C W and Nichols B D. 1981. Volume of fluid (VOF) method for the dynamics of free boundaries. *J. Comput. Phys.* **39**, 201–225.
[36] Han Q Q, Low K W Q, Gu Y, Wang X, Wang L, Song B, Huang C and Setchi R. 2021. The dynamics of reinforced particle migration in laser powder bed fusion of Ni-based composite. *Powder Technol.* **394**, 714–723.
[37] Young Z A, Guo Q L, Parab N D, Zhao C, Qu M L, Escano L I, Fezzaa K, Everhart W, Sun T and Chen L Y. 2020. Types of spatter and their features and formation mechanisms in laser powder bed fusion additive manufacturing process. *Addit. Manuf.* **36**, 101438.
[38] Hu J, Lin X and Hu Y L. 2024. High wear resistance and strength of Hastelloy X reinforced with TiC fabricated by laser powder bed fusion additive manufacturing. *Appl. Surf. Sci.* **648**, 159004.
[39] Wang G et al. 2025. Dispersion hardening using amorphous nanoparticles deployed via additive manufacturing. *Nat. Commun.* **16**, 3589.
[40] Wang C, Yang L, Sheng R-X, Guan S, Bi Z-N, Zhang H, Huang H-L, Jiang L, Zhu -L-L and Zhou X. 2025. In-situ TiC particle-reinforced Hastelloy X superalloy fabricated by laser additive manufacturing. *J. Mater. Res. Technol.* **36**, 1511–1521.
[41] Cox B, Ghayoor M, Pasebani S and Gess J. 2023. Tracking of Marangoni driven motion during laser powder bed fusion. *Powder Technol.* **425**, 118610.
[42] Wang J, Li W, Zhu H H, Zhu X D and Zhang L Q. 2021. Competitive mechanism of phosphorus capturing between MC-carbide (M = Ti, Mo) and ferrite/martensite interface in dual-phase steel. *Mater. Lett.* **283**, 128820.
[43] Liu H, Gu D D, Shi K Y, Zhang H, Li L X, Zhang Y J, Li J Y and Qi J F. 2024. High-strength aluminum alloy processed by micro laser powder bed fusion (μ-LPBF): coordination of laser formability, microstructure evolution, and mechanical properties. *J. Mater. Process. Technol.* **332**, 118580.
[44] Chen J J, Han Y F, Li S P, Wei Z C, Le J W, Shi H G, Huang G F, Lu W J and Zhang D. 2023. Evading the strength and ductility trade-off dilemma in titanium matrix composites through designing bimodal grains and micro-nano reinforcements. *Scr. Mater.* **235**, 115625.
[45] Huang R Z, Zhou Y, Yang Q, Yang X, Wei K, Qu Z, Xie H, Chen X and Fang D. 2025. Localized brittle intergranular cracking and recrystallization-induced blunting in fatigue crack growth of ductile tantalum. *Int. J. Plast.* **186**, 104262.
[46] Wang H L, Ma J, Yuan M N, Liang G, Pei X, Miao Y Z and Li M H. 2022. Microstructure, deformation behaviors and GND density evolution of Ti-Al laminated composites under the incremental compression test. *Mater. Today Commun.* **33**, 104605.
[47] Yang J, Schlenger L M, Nasab M H, Van Petegem S, Marone F, Logé R E and Leinenbach C. 2024. Experimental quantification of inward Marangoni convection and its impact on keyhole threshold in laser powder bed fusion of stainless steel. *Addit. Manuf.* **84**, 104092.
[48] Ratke L and Thieringer W K. 1985. The influence of particle motion on ostwald ripening in liquids. *Acta Metall.* **33**, 1793–1802.
[49] Rani S U, Kesavan D and Kamaraj M. 2023. Possible globularization mechanism in LPBF additively manufactured Ti-6Al-4V alloys. *Mater. Charact.* **205**, 113303.
[50] Du Y, Pestka S A and Elwany A. 2025. Control of spatter due to liquid metal expulsion in additive manufacturing. *Addit. Manuf.* **104**, 104773.
[51] Liu Y-Z, Shi Z-L, Zhang Y-B, Qin M, Hu S-P, Song X-G, Fu W and Lee B-J. 2024. Effect of temperature on the mechanical properties of Ni-based superalloys via molecular dynamics and crystal plasticity. *J. Mater. Sci. Technol.* **203**, 126–142.
[52] Agrawal S, Avadhani G S and Suwas S. 2025. Deformation behaviour of additively manufactured Hastelloy X at high temperatures: the role of concurrent carbide precipitation. *J. Alloys Compd.* **1021**, 179636.
[53] Kitaguchi H S, Small L, Jones I P, Chiu Y L, Hardy M C and Bowen P. 2024. MC decomposition and boride formation in a next generation polycrystalline Ni based superalloy during isothermal exposure at 900 °C. *Mater. Charact.* **209**, 113721.
[54] Zhang H M, Wu Y J, Wang Y, Deng W W, Xu G, Luo K Y and Lu J Z. 2024. In-situ nanoscale precipitation behavior and strengthening mechanism of WC/IN718 composites manufactured by laser powder bed fusion. *Composites B* **284**, 111727.

[55] Sui S et al. 2025. Additive manufacturing of ultrastrong and ductile nickel matrix composites via hetero-deformation induced strengthening. *Int. J. Extrem. Manuf.* **7**, 045003.
[56] Mao D X, Meng X C, Xie Y M, Chang Y X, Qin Z W, Xu S M, Wan L and Huang Y X. 2023. Back stress dynamic balancing strategy enabled strength-ductility synergy in heterostructured Al-SiC composites. *Sci. China Mater.* **66**, 1649–1658.
[57] Feng B, Liu H L, Yang Y, Shen H, Ren Y, Liu Y N, Cui L S, Huang B M and Hao S J. 2024. Endowing low fatigue for elastocaloric effect by refined hierarchical microcomposite in additive manufactured NiTiCuCo alloy. *Int. J. Extrem. Manuf.* **6**, 045501.
[58] Zhang Z H et al. 2025. Anomalous anisotropy in an additively manufactured solid-solution-strengthened superalloy from room to elevated temperatures. *Int. J. Plast.* **192**, 104409.
[59] Zhang Y L, Fang Y J, Jin H Y, Duan Z Y, Yuan Q and Suhr J. 2025. Optimizing the severe strength-ductility trade-off in additively manufactured Ni-free high-N duplex stainless steels via heterogeneous nanoparticles. *J. Mater. Process. Technol.* **342**, 118941.